

Tight Gas Reservoir Simulation: Modeling Discrete Irregular Strata-Bound Fracture Networks and Network Flow, Including Dynamic Recharge from the Matrix

Mark L. McKoy (MMCKOY@FETC.DOE.GOV; 304-285-4426)

W. Neal Sams (WSAMS@FETC.DOE.GOV; 304-285-4068)

EG&G Technical Services of West Virginia, Inc.

P.O. Box 880, 3610 Collins Ferry Rd.

Morgantown, WV 26507



Abstract

The U.S. Department of Energy, Federal Energy Technology Center, has sponsored¹ a project to simulate the behavior of tight, fractured, strata-bound gas reservoirs that arise from irregular, discontinuous, or clustered networks of fractures. New FORTRAN codes have been developed to generate fracture networks, to simulate reservoir drainage/recharge, and to plot the fracture networks and reservoir pressures. Ancillary codes assist with raw data analysis.

FRACGEN, the fracture network generator, implements four Boolean models of increasing complexity through a Monte Carlo process that samples fitted statistical distributions for various network attributes of each fracture set. Three models account for hierarchical relations among fracture sets, and two generate fracture swarming. Termination/intersection frequencies may be controlled implicitly or explicitly.

Using an output file consisting of fracture end-point coordinates and apertures, NFFLOW, the flow simulator, then computes the transient flow rates or bottom-hole pressures according to user-specified pressure or rate schedules, respectively. The flow simulator divides each matrix block into subregions that drain to the midpoint of the adjacent fracture segments in accordance with a one-dimensional, unsteady-flow model. Each idealization approximates both the volume and the mean flow path of each subregion. There is no flow from matrix block to matrix block. Volumetric flow rate in the fractures is modeled as a linear (cubic law) function of the pressure difference between the recharge points and the fracture intersections. The linear function incorporates a "real gas pseudopotential," which allows viscosity and the z-factor to vary with pressure. A requirement of material balance among all intersections couples the individual recharge models together. The resulting equations for material balance at fracture intersections are solved by a Newton-Raphson technique that accommodates a slight nonlinearity caused by matrix recharge. A network consisting of 2300 fractures and 51 time steps was simulated in less than 1 hour (clock time) on a Pentium 200 equivalent computer.

¹Research Sponsored by the U.S. Department of Energy's Federal Energy Technology Center, under contract DE-AC21-95MC31346 with EG&G Technical Services of West Virginia, Inc., 3604 Collins Ferry Rd., Morgantown, WV 26505-2353; telefax: 304-599-8904.

Introduction

Beginning in the late 1970s, investigators of fractured aquifers began to statistically describe fracture networks for purposes of flow simulation. Initial attempts were simple. Networks were generated in a Boolean process in which fractures were randomly located and fracture length, aperture, and orientation were assigned as either fixed variables or as members of simple statistical distributions (i.e., uniform distributions, Gaussian distributions, or lognormal distributions) (see, e.g., Baecher et al., 1977). Flow simulation of these discrete irregular networks began during the early 1980s and was limited to small numbers of fractures that carried flow under steady-state conditions without matrix participation (e.g., Long et al., 1982).

Throughout the 1980s, development of irregular fracture network generators and flow simulators accelerated. This decade saw the advent of three-dimensional modeling, spatial correlation, flow simulation via several techniques, and contaminant transport modeling (see generally Bear, Tsang and de Marsily, 1993). Most of the computer programs, however, implemented aquifer models designed for investigation of either proposed radioactive waste repository sites or geothermal hard-rock reservoirs (e.g., "FRACMAN/MAFIC" by Golder Associates, Seattle, USA; "NAPSAC" by AEA Decommissioning & Radwaste, Harwell, United Kingdom; "FMG" and an equivalent discontinuum model by Lawrence Berkeley Laboratories, Berkeley, USA; "FRACNET" by Robinson, 1989). These models do not serve the needs of the petroleum industry because they do not model strata-bound fracture networks, matrix storage of hydrocarbons, or hydrocarbon flow. Other models that might serve the needs of the petroleum industry were either conceptual or were prototypes that were not sufficiently developed for practical widespread use. More useful programs for modeling petroleum reservoirs have appeared during the 1990s (e.g., new versions of FRACMAN by Golder Associates; hierarchical modeling of fracture networks in stratified rock by Gervais et al., 1992).

Is modeling flow in discrete irregular fracture networks worth the perceived extra costs (of time, data, and computer resources) in comparison to the various continuum and porous media approaches? The answer is yes, for the following reason. Networks and fractures themselves usually present large permeability anisotropies and heterogeneities across a range of scales. Thus, the scale of observation and spatial variability become critical issues in every investigation, and simple averaging, as required by conventional models, tends to lose utility.

To demonstrate the need for cluster modeling of discrete fractures, the real or predicted properties of fracture networks have been abstracted frequently in recent years for use in models of anisotropic heterogeneous porous media where fractures or fracture swarms are represented as zones of greater intergranular permeability. Proper abstraction requires additional work that could be avoided if the fracture data are merely summarized and input directly.

As if large-scale flow-path geometry and statistical abstraction failed to provide enough complexity, analysts and reservoir producers must contend with stress sensitivity and plugging of fractures by fluids from drilling or stimulation. These two issues require near-bore simulation studies that account for smaller-scale near-bore variations in irregular networks -- things not readily accounted for by conventional models.

The fracture network models presented here represent fracture networks in two-dimensional space and in patterns that are either random or clustered but without larger-scale spatial correlation. All fractures are assumed to extend perpendicular to the reservoir layer from top to bottom of the layer. Where fracture patterns vary significantly in the third dimension (perpendicular to the bedding plane) or where the fracture locations are either regular or uniform, three-dimensional models or conventional models might be more appropriate. Likewise, where the model must account for larger-scale spatial correlation of fractures around major structural features, such as large folds or faults, other models might be more appropriate. Our fracture network models best represent regional fractures (including swarms) and simple clusters of tectonic fractures.

To account for dynamic matrix drainage to (or recharge from) the fracture network, a new flow simulator was produced. The most salient features of this simulator are as follows. It computes transient flow rates or bottom hole pressures according to user specified pressure or rate schedules. It handles wells that are horizontal (including multilaterals), inclined, or vertical and that are either hydrofractured or intersected by natural fractures. Flow is single phase, and gravity effects are neglected. Only one reservoir layer is modeled, and no flow occurs across the upper and lower boundaries of the reservoir layer. There are no assumptions about the configuration of the fracture network other than that it is represented two-dimensionally by a file that lists end point coordinates and an aperture for each fracture on a separate line of input data.

Fracture-bound matrix blocks are subdivided into subregions that drain to (or recharge from) the midpoint of adjacent fractures in accordance with a one-dimensional unsteady-flow model. There is no flow from matrix block to matrix block. Volumetric flow rate within the fractures is modeled as a linear (cubic law) function of the pressure difference between the recharge points and the fracture intersections. A requirement of material balance between all the intersections couples the individual recharge models together. The resulting equations for mass balance at intersections are solved by a Newton-Raphson technique that accommodates the slight non-linearity caused by the matrix participation. All flow towards the well occurs through the fractures, except for drainage from matrix blocks directly contacting the well bore.

Fracture Network Generation

Objectives: 2-D Strata-Bound Networks with Fracture Swarming

This project began with the goal of modeling Devonian shale reservoirs of the Big Sandy field, such as the reservoir tapped by the U.S. Department of Energy's RET #1 well in Wayne County, West Virginia. At this site, the available data on fracture spacing and relative fracture location came from short core segments and from a borehole video of the RET #1 well's horizontal bore. Thus, the first objective was to *generate a useful model of the fracture network from an essentially one-dimensional sample* of the reservoir.

Neither the lengths nor the intersection/termination frequencies of fractures could be observed, either in the reservoir or in nearby analog outcrops. Fractures intersecting the well were obviously clustered. Maximum influx of gas occurred within these clusters, so *modeling clusters of fractures* became the second objective. However, like fractures, neither the lengths nor the

intersection/termination frequencies of clusters could be observed. Furthermore, suitable simple schemes to model clusters of fractures in strata-bound rocks were not found in the literature. Therefore, we focused on making two-dimensional models of strata-bound fractures that were located either randomly or in swarms.

To estimate fracture lengths, the initial plan was to start modeling with short fractures and gradually increase the fracture length with each new series of fracture networks that would be generated, until flow simulation results began to match the well production or well test results. Fracture center-point density would be decreased while fracture length would be increased so that fracture density would remain constant. Cluster lengths might be estimated in a similar manner with longer-term production data. Intersection/termination frequencies would be ignored because these attributes could not be determined with data from wells. This initial plan was not implemented because the flow simulator was not yet operational.

Later, a more successful reservoir modeling effort began with an attempt to simulate a well test at the U.S. Department of Energy's Multi-Well Experiment (MWX) site near Rifle, Colorado. Information on fracture lengths and intersection/termination frequencies was available for some sets from Lorenz et al. (1989, 1991) and from their analog outcrop fracture map (Figure 3A of Lorenz and Finley, 1991). It became apparent that this analog outcrop could provide essential bits of information for the generation of synthetic fracture networks that match the real networks in nearby deeply buried reservoirs.

It also became apparent that, even where analog outcrops are unavailable and where reservoir fracture lengths cannot be readily estimated from traditional correlations with bed thickness, geological interpretation of fracture sets and well test data could suggest certain characteristic intersection/termination frequencies that would require determinable fracture lengths. Intersection/termination frequencies not only are useful for estimating fracture length distributions in reservoirs; they also are essential to properly model flow and network appearance. Our early flow simulation work demonstrated that it was insufficient to merely know the fracture length distributions in reservoirs and to plot fractures with those lengths in a Poisson or mixed Poisson process. It is imperative also to control intersection/termination frequencies, because a network's connectivity affects flow rates through time. Therefore, *modeling connectivity* became the third objective of the fracture network modeling effort.

Many tight gas reservoirs exist in relatively thin strata, where many of the largest and most conductive fractures extend from top to bottom in individual beds, but do not extend into adjacent beds because of contrast in rheological properties. Therefore, two-dimensional representations of strata-bound fracture networks may adequately represent many reservoirs. Where many fractures extend into adjacent beds and where a large flux of gas occurs across bed boundaries, three-dimensional models are needed.

Approach: Statistical Models

The currently popular techniques of geostatistics (e.g., Kriging and sequential indicator simulation) depend on the application of a certain support area, usually a square or rectangle. Unless an extremely fine-grid representation is used, these techniques fail to accommodate the irregular

shapes of relatively small but potentially important geologic phenomena such as fractures and clusters. These techniques also fail to accommodate scale-dependent attributes such as fracture permeability, which cannot be represented easily with areal or volumetric averages. Boolean techniques, on the other hand, readily permit modeling of objects across a range of scales when the various attributes of the objects can be described with distributions or probabilities. A critical drawback of Boolean techniques is their failure to account for spatial correlation between objects. However, conditional simulation and synthetic annealing may be used with Boolean models to match observed fracture/cluster locations and to develop spatial correlation.

As in numerous previous studies by various investigators, we apply a stochastic Boolean approach to modeling fracture networks. In our simplest models, fractures are generated by randomly selecting fracture center-points and then assigning a length, aperture, and orientation to each center-point to define each fracture. Fracture attributes are defined by fixed variables and statistical distributions, as shown in Tables 1 and 2. Our simplest models are similar to those presented by the earliest investigators. In our more complex models, shown in Tables 3 and 4, fractures may be placed within swarm-like clusters. In all four models, fractures may be moved to locations where the specified termination frequencies are achieved. Thus, local spatial correlation arises from these processes for control of clustering and connectivity. The discussion below introduces the most important distributions chosen to generate two-dimensional representations of fracture network geometry from a one-dimensional sample of fractures.

Table 1. Fracture Network Model for Level 1	
Network Attribute	Distributions ¹
number of sets	0
fracture orientations	random
fracture locations ²	random
fracture lengths ³	continuous uniform (l_{\min}, l_{\max}) discrete uniform (l_{\min}, l_{\max}) continuous nonuniform (l_{\min}, l_{\max})
fracture apertures	fixed variable (W)
fracture densities	fixed variable (D)
fracture termination	implicit (via end-point shifting) (%) explicit (via “synthetic annealing”) (%)
¹ Variables explained in Table 5.	
² Parent-daughter clustering can be induced by the “synthetic annealing” routine and “end-point shifting.”	
³ Length distributions will be modified by termination control processes.	

Table 2. Fracture Network Model for Level 2	
Network Attribute	Distributions ¹
number of sets	$i = 1$ to 10
fracture orientations	Gaussian ($\theta_i, s_{\theta i}$)
fracture locations ²	random
fracture lengths ³	continuous uniform ($l_{i,\min}, l_{i,\max}$) discrete uniform ($l_{i,\min}, l_{i,\max}$) continuous nonuniform ($l_{i,\min}, l_{i,\max}$) intersection freq. controlled ($l_i, l_{i,\max}$)
fracture apertures	fixed variable (W_i)
fracture densities	fixed variable (D_i)
fracture termination frequencies	implicit (via end-point shifting) (%) explicit (via "synthetic annealing") (%)
fracture intersection frequencies	explicit (via "synthetic annealing") (%)
¹ Variables explained in Table 5. ² Parent-daughter clustering can be induced by the "synthetic annealing" routine and "end-point shifting." ³ Length distributions will be modified by termination and intersection control processes.	

Table 3. Fracture Network Model for Level 3	
Network Attribute	Distributions ¹
number of sets	$i = 1$ to 10
fracture orientations	Gaussian ($\theta_i, s_{\theta i}$)
cluster orientations	Gaussian ($\theta_{ci}, s_{\theta ci}$)
cluster locations ²	random
fracture locations ²	parallel to cluster axis - random normal to cluster axis - exponential (m_i)
fracture lengths ³	continuous uniform ($l_{i,\min}, l_{i,\max}$) continuous nonuniform ($l_{i,\min}, l_{i,\max}$) discrete uniform ($l_{i,\min}, l_{i,\max}$) intersection freq. controlled ($l_i, l_{i,\max}$)
cluster lengths ³	continuous uniform ($l_{ci,\min}, l_{ci,\max}$)
fracture apertures	fixed variable (W_i)

Table 3. Fracture Network Model for Level 3 (Continued)	
fracture densities	fixed variable intracluster density (D_{ci})
cluster densities	fixed variable (D_{ci})
fracture termination frequencies	implicit (via end-point shifting) (%) explicit (via "synthetic annealing") (%)
fracture intersection frequencies	explicit (via "synthetic annealing") (%)
cluster termination frequencies	implicit (via end-point shifting) (%)
¹ Variables are explained in Table 5. ² Parent-daughter clustering can be induced by the "synthetic annealing" routine and "end-point shifting." ³ Length distributions will be modified by termination and intersection control processes.	

Table 4. Fracture Network Model for Level 4	
Network Attribute	Distributions ¹
number of sets	$i = 1$ to 10
fracture orientations	Gaussian ($\theta_i, s_{\theta i}$)
cluster orientations	Gaussian ($\theta_{ci}, s_{\theta ci}$)
cluster locations ²	random
fracture locations ²	parallel to cluster axis - random normal to cluster axis - exponential (m_i)
fracture lengths ³	lognormal (l_i, s_{li}) continuous uniform ($l_{i,min}, l_{i,max}$) discrete uniform ($l_{i,min}, l_{i,max}$) intersection frequency controlled (l_i, s_{li})
cluster lengths ³	lognormal (l_{ci}, s_{lci})
fracture apertures	lognormal (w_i, s_{wi})
fracture densities	lognormal intracluster densities (d_i, s_{di})
cluster densities	fixed variable (D_{ci})
fracture termination frequencies	implicit (via end-point shifting) (%) explicit (via "synthetic annealing") (%)
fracture intersection frequencies	explicit (via "synthetic annealing") (%)
cluster termination frequencies	implicit (via end-point shifting) (%)
¹ Variables explained in Table 5. ² Parent-daughter clustering can be induced by the "synthetic annealing" routine and "end-point shifting." ³ Length distributions will be modified by termination and intersection control processes.	

Table 5. Variables Incorporated in the Stochastic Fracture Models.

Subscripts

i	a particular fracture set.
k	a particular cluster.
j	a particular fracture.
c	clusters or fracture zones, generally.
z	intra-cluster fracture center-point density.
θ	orientation.
max	maximum value.
min	minimum value.

Note: all other subscripts and subscripted symbols will be explained in the text where used.

Fixed Variables

L	effective dimension of fracture zones or fractures (ft).
W	effective hydraulic aperture (width) of fractures (ft).
D	number of fracture or fracture zone center-points per unit representative area (pts/ft ²).

Statistics

θ	orientation (degrees).
d	effective intra-cluster fracture center-point density (pts/ft ²).
l	effective length of fractures or fracture zones (ft).
m	distance between fractures and axis of fracture zone (ft).
w	effective aperture (width) of fractures (ft).
s	standard deviation about the mean for any parameter (as denoted by subscript).

We begin to derive our fracture network models by assuming that an investigator can treat fractures as straight line segments (or rectangles in three-dimensional space) that are defined by a center point, a length, and an azimuth (all fractures are perpendicular to bedding). We can analyze separately the spatial arrangement of center points, orientations, and length dimensions. We assume that fractures, when clustered, occur in "swarms." In nature, swarms tend to be long, sometimes sinuous, perhaps strata-bound zones with maximum fracture density near their centers. So, we can treat clusters as linear zones that are defined by a center point, a length, a width, and an orientation. Again, we can analyze separately the spatial arrangement of center points, orientations, and length-width dimensions for clusters. Intracluster fracture center-point density can be determined after cluster dimensions are defined. Fracture apertures are assigned after the lines (representing fractures) are generated. Each attribute must be analyzed and modeled with respect to an assumed theoretical distribution, unless frequency distributions are input directly.

Except by design, field work rarely yields enough information to study the spatial arrangement of fracture and cluster center-points. More often, investigators determine the number and location of fractures or clusters encountered along a straight sample line (e.g., a well bore, mine shaft, or road cut). Investigators typically calculate the average distance between fractures and report this value as the fracture spacing. However, fracture spacing more appropriately refers to a distri-

bution of distances between fractures, measured perpendicular to the mean orientation of the fracture planes belonging to one set, if sets exist. The distribution of fracture spacing is then analyzed, assuming various models, to estimate the density and the two-dimensional or three-dimensional spatial arrangement of fractures.

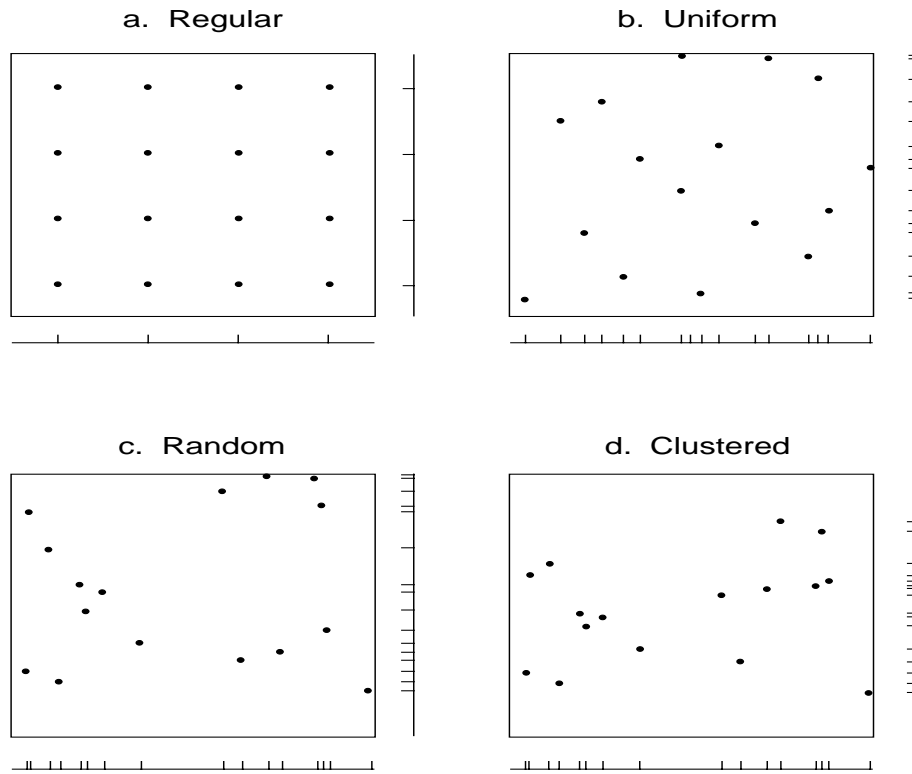
Figure 1 illustrates the fundamental two-dimensional patterns of points in space. These patterns and the associated probability distributions are described in statistics textbooks. On the bottom and right sides of each two-dimensional illustration, Figure 1 shows the equivalent one-dimensional pattern of point locations. Think of the one-dimensional patterns as the patterns that would arise if the points in the two-dimensional illustrations were converted into lines (fractures) oriented perpendicular to the one-dimensional illustrations (which would represent sample lines). Figure 2 presents relative frequency histograms for the fundamental distributions of spacing, as observed along a sample line. These distributions of spacing arise from the fundamental patterns of point location.

When a reservoir exhibits fixed values of spacing (Figure 2a) or triangular distributions of spacing (Figure 2b) for each set, as observed in core or borehole imagery, the investigator should apply a conventional dual-permeability simulator. Thus, fixed values of spacing (indicating regular fracture patterns) and triangular distributions of spacing (indicating uniform fracture patterns) will not be considered further. Our objective is to model fractures that are randomly located or clustered into swarms. Fracture swarms have been observed frequently in basins around the world (see Laubach, 1992, for examples from the Piceance Basin, Green River Basin, and San Juan Basin).

The pattern of points on a map is "random" (Figure 1c) if each quadrat has the same probability of containing a center point as all other quadrats of equal size and if all points are placed without regard to the placement of other points. The distribution of spacing between random points along a sample line is exponential (Figure 2c), with more short spacings than long spacings. Ostensibly, sedimentary rock can develop a truly random spacing of fractures only where the stress field is truly homogeneous and where randomly located, small-scale heterogeneities exist in the rock. In nature, things tend to be related, and fractures develop more closely together in some areas because of stress variations around primary or structural features in the rock or because of local stress variations originating in the underlying rock. In other areas, fractures are more uniformly spaced because each fracture relieved the ambient stress as it formed. Consequently, truly random fracture locations in rock are probably rare. Locations that appear random probably result from a combination of a uniform distribution and a clustered distribution.

The probability distribution applied to randomly located points in space is a Poisson distribution. The Poisson distribution is a discrete distribution consisting of events or objects that may be counted in defined areas of space. For example, if a reservoir is divided into q equal-sized quadrats, each of area a , such that the number of quadrats is approximately equal to the total number of fracture center-points, n , the Poisson probability function will tell us the probability that a quadrat will contain exactly x fracture centers:

$$p(x) = \chi^x e^{-\chi}/x!, \quad (1)$$



M93002636

Figure 1. Fundamental spatial patterns of points (1-D & 2-D).

where $0.5 < n/q < 5$, and where χ represents both the mean number of fracture centers per quadrat (i.e., n/q) and the variance about this mean.

A sample mean may be calculated with

$$\chi = n/q, \quad (2)$$

and the sample variance with

$$s^2 = \sum_{i=1}^q (x_i - n/q)^2 / (q - 1), \quad (3)$$

where x_i is the number of events or objects (i.e., fracture centers) in the i th quadrat.

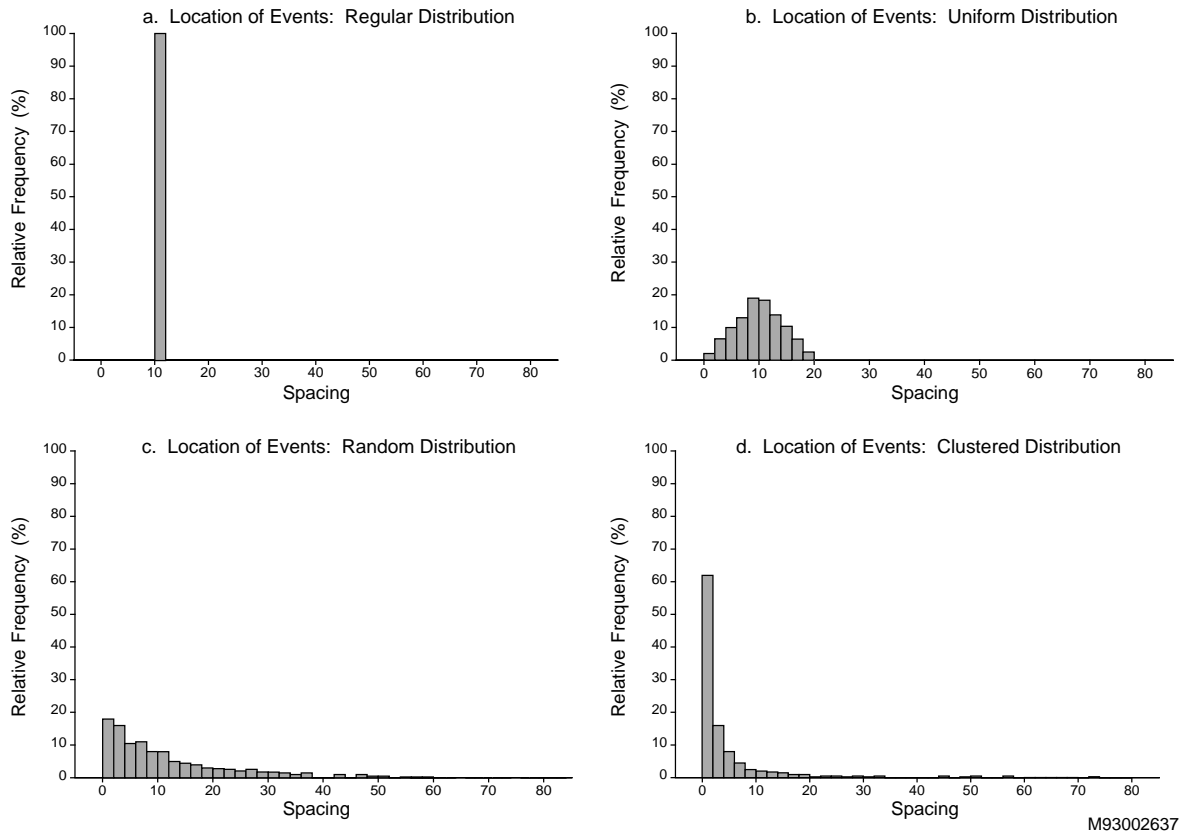


Figure 2. Fundamental distributions of spacing that arise from the fundamental spatial patterns of points.

The sample's variance in the number of fractures per quadrat, s^2 , should approximately equal the mean if the pattern of fractures is truly random. If the sample's variance is much larger than the mean, the pattern is more clustered than random; if much less than the mean, the pattern is more uniform than random.

Randomly located points may appear clustered, but they are not. The pattern of points on a map is "clustered" (Figure 1d) if equal-size quadrats have different probabilities of containing a center point and if any points are placed in relation to the placement of other points. From an intuitive standpoint, the theoretical distribution for the spacing of clustered events along a sample line appears to be some variety of exponential distribution (perhaps a Weibull distribution), which accounts for the degree of clustering. As the points become more tightly clustered, the distribution of spacing changes from a classical exponential distribution (arising from randomly located objects) to some exaggerated form of an exponential distribution (Figure 2d).

Clustered point patterns are generally modeled as combinations of two or more distributions. A popular model is the negative binomial distribution, which is a combination of a Poisson distribution and a logarithmic distribution. In this combination, the clusters or zones are randomly

located in space, the numbers of fractures within clusters are distributed logarithmically, and the degree of clustering is accounted for by a clustering parameter. However, the negative binomial distribution does not specifically account for anisotropic or elongated clusters.

The cluster models presented here parallel the negative binomial model but also account for the elongation and anisotropy of fracture swarms. We have not derived a mathematical probability function for our model, so we can only describe the combinations of distributions. First, the centers of fracture zones are chosen in a Poisson process (overlap of clusters is not prevented). The distance between each fracture center-point and the axis of the zone is selected from an exponential distribution, which has a mean value that acts as a clustering parameter and which determines cluster width. The density of fracture center-points within clusters is either constant or lognormal, and cluster lengths are either random (within limits) or lognormal, respectively. So, the numbers of fractures per cluster are distributed either randomly or logarithmically.

It is possible to model clustered fractures in bedrock as either a regular or a uniform pattern of fractures with a lognormal distribution of spatially correlated apertures, and these models might fit some reservoirs nicely. However, we chose to apply randomly located *fractures* in the simpler models and randomly located *clusters* in the more complicated models. Modeling fractures as randomly located clusters is consistent with the expected pattern of fractures in the typical basin where the sedimentary rock sequence is extremely heterogeneous and where paleo-stress fields varied on a local scale but where major compressional folds did not develop.

It is also reasonable to use randomly located cluster patterns when the spatial correlation of fracture zones cannot be determined from the available information (as frequently occurs). Clusters produced by this model should mimic simple fracture swarms produced by noncompressional (drape) folding, minor faulting, and internal stress irregularities developed around primary rock heterogeneities. Our clusters may not accurately mimic the larger-scale spatial pattern found around major compressional folds and large tectonic faults. Nevertheless, our cluster models do provide a first-order approximation of the fracture patterns of these structures, and they are useful for modeling fractures within small areas on these structures.

The choice of theoretical distributions is an important issue, not only in modeling fracture locations, but also for modeling fracture and cluster orientations. The most appropriate probability model for a "clustered" distribution of fracture orientations in two-dimensional space is the Von Mises distribution, also known as the "circular normal" distribution. However, we can use a Gaussian distribution instead of a Von Mises distribution because the Von Mises probability function becomes asymptotic to the Gaussian probability function as the range and the variance of the distribution approaches zero. As a rule, when a distribution is nearly symmetrical and the range is less than 90 degrees, the Gaussian mean will differ from the mean angle by less than 1 degree; and when the range is less than 60 degrees, the standard deviation will differ from the angular deviation by less than 1 degree (Batschelet, 1965). We anticipate no problems with the use of a Gaussian approximation because fractures tend to occur in sets that nearly always have a range less than 60 degrees.

As mentioned, our models also require statistical distributions for fracture length, fracture aperture, cluster length, the location of fractures within clusters, and the density of fractures

within clusters. For our most complex model, we adopt the lognormal distribution for fracture length, fracture aperture, cluster length, and the density of fractures within clusters. Many continuous distributions in nature have the property that most of the observations drawn from the population have a small magnitude while a few have a large magnitude (e.g., gold content of stream sediment samples). Such a distribution fits, at least on first impression, the measured aperture of fractures, the measured lengths of fractures, and the measured lengths of fracture zones. Please note that such lognormal appearance, rather than a power-law appearance, may result entirely from a scale-dependent sampling bias or censoring. But given the common occurrence of bias and censoring during sampling, the lognormal distribution often fits the available data. The lognormal probability density function is

$$p(x) = \frac{1}{x s_u (2\pi)^{1/2}} \exp\left(-(\ln(x) - U)^2 / 2s_u^2\right), \quad (4)$$

where U and s_u^2 are the mean and variance, respectively, of the natural logarithms of the measurements of x . The lognormal mean of x is given by

$$\chi = \exp(U + 0.5s_u^2), \quad (5)$$

and the lognormal variance of x is given by

$$s_x^2 = \chi^2(\exp(s_u^2) - 1). \quad (6)$$

For the distance between fractures and their cluster axis, we adopt the exponential distribution. Exponential distributions describe situations where the probability of an event decreases over time or space and the rate of change in the probability is directly proportional to the probability at that instant or location. Such distributions are analogous to the familiar laws of decay. Within the family of exponential distributions, there are single-parameter distributions, such as the one presented below, and there are dual-parameter distributions, such as the Weibull distribution and the gamma distribution. For simplicity, we apply the most commonly used, single-parameter density function:

$$p(x) = (1/\chi) \exp(-x/\chi), \quad (7)$$

where χ is both the exponential mean and the exponential standard deviation of the population. The user may estimate the population mean with a sample mean calculated as either an arithmetic average or as the sixty-third percentile (63%) value of the sample observations, ranked from least to greatest. By adopting the one-parameter distribution, we have only one parameter to control clustering (analogous to the negative binomial distribution).

For the placement of fractures along the axes of clusters, we adopt a combination of a continuous uniform (random) distribution and one of several fracture length distributions. Three to four fracture length distributions are available in each model. The distributions are: continuous uniform, discrete uniform, continuous nonuniform, lognormal, and intersection frequency controlled.

The continuous uniform probability density function is

$$p(x) = 1 / (b - a) , \quad (8)$$

and the probability distribution function is

$$P(x) = (x - a) / (b - a), \quad (9)$$

where the mean of x is

$$\chi = (b + a) / 2 . \quad (10)$$

The lower and upper limits of the distribution are a and b , respectively.

The lognormal distribution was presented above. Probability density and distribution functions will not be presented here for the other three length distributions because they are not central to understanding the fracture network models and are not required for the derivation of any equations presented below. Furthermore, they serve little useful purpose in the analysis of the input data (e.g., goodness-of-fit tests).

Both the discrete uniform distribution and the continuous nonuniform distribution are symmetric, so fracture center-point density distributions within a cluster can be handled the same way as for the continuous uniform distribution. Both distributions are characterized by lower and upper limits of the distribution, a and b , and both can have a mean value estimated with Eq. 10. In nature, fractures never have uniform distributions of length, and our use of a uniform distribution is a gross (but often helpful) simplification. Fracture lengths are the products of local stress fields, interacting fracture growth (stress field interference), and initiation stress requirements, especially for fractures attempting to propagate across pre-existing fractures. Late-forming fractures tend to have lengths related to the spacing of early-formed fractures and to their capacity to propagate across early-formed fractures. For these reasons, an intersection frequency-controlled distribution (at a given scale of observation) will tend to have a nonsymmetric, lognormal shape; so we adopt the lognormal probability distribution as a proxy and a lognormal mean as a measure of central tendency for this distribution.

Given that the number of unbiased measurements needed to calculate the required statistics are difficult to obtain, for lower-level models we adopt fixed variables to describe fracture aperture and intracluster fracture center-point density.

The approach to modeling connectivity in a fracture network is, perhaps, less amenable to the Boolean technique. Theoretical discrete distributions appropriate for modeling T-termination frequencies and intersection frequencies have not been found. Therefore, these observed frequency distributions are input directly for explicit modeling. If the connectivity attributes of a network are modeled, hierarchical relationships among fracture sets can be created by generating each set independently and in chronological order.

Overview of Fracture Network Modeling

The preceding section introduced the theoretical distributions upon which the models (Levels 1 through 4) are based. The method of fracture pattern generation is summarized below only for the Level 2 and Level 4 models. Connectivity control methods are described after describing the basic generation process.

Level 2

The Level 2 model generates randomly located fractures as sets. Each fracture set is defined by its orientation distribution, fracture length distribution, effective fracture aperture (W_i), and density of center points (D_i).

A standard procedure is used to generate Gaussian distributions, such as orientation. A random number between zero and one is generated and treated as a cumulative probability. FRACGEN applies a fitted fifth-degree standard rational equation to estimate standard normal deviates as a function of cumulative probability. Standard normal deviates less than -3.0 or greater than +3.0 are reassigned values of -3.0 or +3.0, respectively. Each standard normal deviate is converted to an observation by

$$x_{i,j} = \chi_i + z_{i,j} s_i, \quad (11)$$

where $x_{i,j}$ is the j th observation (i.e., orientation) in the i th set; χ_i is the mean of the i th set (e.g., θ_i); $z_{i,j}$ is the j th standard normal deviate in the i th set (determined from the j th random number generated); and s_i is the standard deviation of the i th set (e.g., s_{θ_i}).

Fracture patterns for the Level 2 model are generated by randomly selecting an x-coordinate and a y-coordinate for the center point of each fracture. Fractures are generated until the number of center points in the generation region provides the given density, D_i . To make fractures, each center point is assigned a fracture length from a user-selected distribution. There are four length distribution options. The default is a continuous uniform distribution, in which each fracture is randomly assigned a length between the specified limits.

Alternatively, the user may choose a discrete uniform distribution, in which fractures are plotted by rank, starting with the longest fractures. This creates a mesh of long fractures upon which the shorter fractures in the same set can terminate. The user may also choose a continuous nonuniform distribution, in which the range of lengths varies about the mean. This option is intended for use with the fracture termination control process to help control the frequency of unconnected

short fractures without changing the mean fracture length. The user may also choose an intersection frequency-controlled fracture length distribution, defined by a lognormal mean length (input as $l_{i,min}$) and a maximum length ($l_{i,max}$).

After assigning a length, each fracture is oriented based on a Gaussian mean and standard deviation. Each fracture is then assigned the average effective aperture, W_i . After fractures are generated for the first fracture set, they are generated for the second, third, ..., and i th fracture set.

The user must supply the input data file with the parameters shown in Table 2 plus the dimensions of the flow region. The flow region has been enclosed within a fracture generation region, which is defined to extend a distance equal to the maximum fracture length (of the i th set) beyond the boundaries of the flow region. For a set with an extremely low center-point density, the generation region expands to accommodate at least five fractures.

Level 4

The Level 4 model generates sets of clustered fractures, like the Level 3 model, and introduces lognormal distributions for several attributes to better represent the inherent network heterogeneity of real fracture networks. All fractures are plotted as members of clusters that have a lognormal distribution of intracluster fracture center-point densities defined by d_i and s_{di} .

The lognormal distributions are generated in a procedure analogous to the procedure for generating a Gaussian distribution. First, a standard normal deviate is generated. Standard normal deviates less than -3.0 or greater than +3.0 are reassigned values of -3.0 or +3.0, respectively. Then, the standard normal deviate is converted into a lognormally distributed observation by

$$U = \ln(\chi_i) - 0.5\ln((s_x^2/\chi_i^2)+1) , \quad (12)$$

$$s_u = [\ln((s_x^2/\chi_i^2)+1)]^{1/2} , \text{ and} \quad (13)$$

$$x_{i,j} = \exp(z_{i,j} s_u + U) , \quad (14)$$

where U and s_u are, respectively, the mean and the standard deviation of the natural logarithms of the sample of x for the i th set; χ_i is the lognormal mean of x (Eq. 5); s_x is the lognormal standard deviation of x (see Eq. 6); $x_{i,j}$ is the j th observation (e.g., length of a fracture) in the i th set produced in the model; and $z_{i,j}$ is the j th standard normal deviate (determined from the j th random number generated).

Fracture patterns for the Level 4 model are generated by randomly selecting an x-coordinate and a y-coordinate within the generation region for each cluster's center-point. Clusters are generated until the number of cluster center-points within the generation region provides the given cluster density, D_{ci} , for the i th cluster set. To make clusters, each center point is assigned an axial orientation based on the mean orientation and standard deviation for the i th fracture set, unless

statistics for the orientation of clusters are specifically supplied. Each cluster's length ($l_{ci,k}$) is selected from a lognormal distribution, and cluster end-points are calculated. If desired, cluster end-points are shifted, within user-specified limits (as a percent of cluster length), to points of intersection with pre-existing clusters. Each cluster's width (L_{wi}) and number of fractures ($N_{i,k}$) are defined as follows².

$$L_{wi} = 12 m_i . \quad (15)$$

For $l_{ci,k} \geq l_{i,2.0}$

$$N_{i,k} = d_{i,k} L_{wi} [l_{ci,k} - l_{i,2.0} + \kappa_1 (l_{i,2.0} - l_{i,-3.0})] , \quad (16)$$

and for $l_{ci,k} < l_{i,2.0}$

$$N_{i,k} = d_{i,k} L_{wi} \kappa_2 (l_{ci,k} - l_{i,-3.0}) , \quad (17)$$

where

$$\kappa \approx \frac{1}{B+1} \sum_{j=0}^B \left[\frac{1}{s_u (2\pi)^{1/2}} \int_0^{x_j} \frac{1}{l} \exp \left[\frac{-(\ln(l)-U)^2}{2s_u^2} \right] dl \right] , \quad (18)$$

where

$$x_j = l_{i,-3.0} + j\Delta x , \quad (19)$$

where for κ_1 ,

$$\Delta x = (l_{i,2.0} - l_{i,-3.0}) / B , \quad (20)$$

and for κ_2 ,

²For non-skewed fracture length distributions, the number of fractures per clusters is

$$N_{i,k} = D_{zi} L_{wi} (l_{ci,k} - (l_{i,\max} + l_{i,\min}) / 2), \text{ where } l_{ci,k} \geq l_{i,\max}$$

$$N_{i,k} = D_{zi} L_{wi} (l_{ci,k} - l_{i,\min})^2 / 2(l_{i,\max} - l_{i,\min}), \text{ where } l_{ci,k} < l_{i,\max}$$

$$\Delta x = (l_{ci,k} - l_{i,-3.0}) / B , \quad (21)$$

where

B = arbitrarily selected number of intervals.

Critical fracture length parameters are calculated as

$$l_{i,-3.0} = \exp (U - 3s_u) \quad (22)$$

and

$$l_{i,2.0} = \exp (U + 2s_u) , \quad (23)$$

where

$$U = \ln(l_i) - 0.5\ln((s_u^2/l_i^2)+1) \quad (24)$$

and

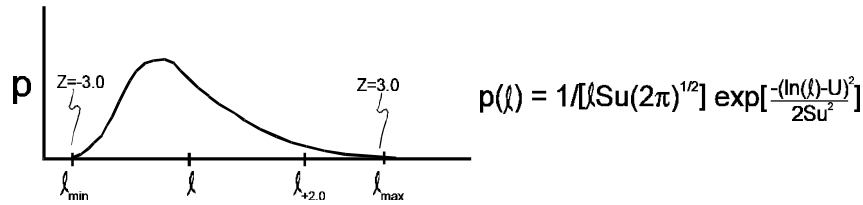
$$s_u = [\ln((s_u^2/l_i^2)+1)]^{1/2} . \quad (25)$$

Cluster width as defined above will contain 99.8 percent of the fractures generated. The parameter $l_{i,2.0}$ is the fracture length two standard deviations above the mean; $l_{i,3.0}$ is the length three standard deviations above the mean. Please note that $l_{i,2.0}$ has been substituted for $l_{i,3.0}$ to reduce the amount of time-consuming numerical integration by FRACGEN. Consequently, the equations presented above slightly overestimate the theoretically correct number of fractures for each cluster. Figure 3 illustrates intracluster fracture center-point density and its relationship to fracture length. The κ function, shown in Eq. 18, estimates the fraction (or weight) that upon multiplication with $d_{i,k}$ gives the weighted average center-point density in the regions of reduced density at each end of a cluster (see Figure 3b).

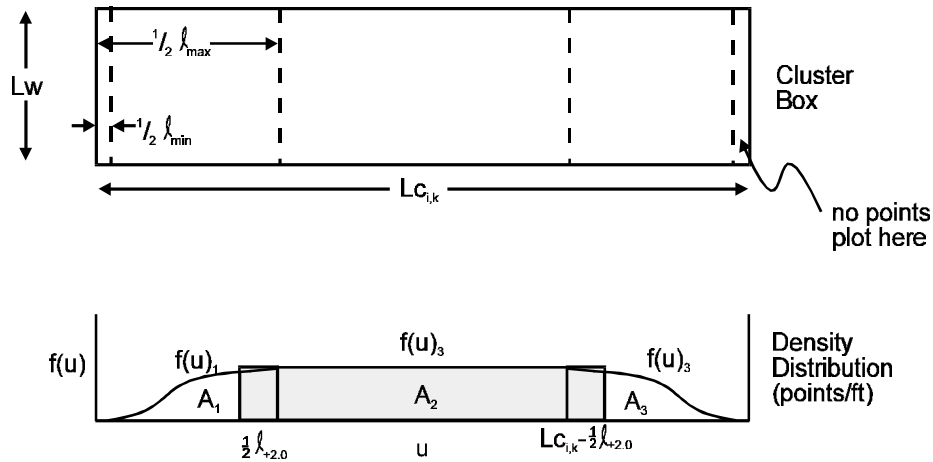
Each cluster's length and width serve to define a local coordinate system -- coordinates u and v , respectively. Each fracture's center point is positioned randomly along the axis of the cluster (coordinate u):

$$u_{ij} = 1/2 l_{ij} + R_{jl} (l_{ci,k} - l_{ij}) . \quad (26)$$

A. Distribution of Fracture Lengths (ℓ):



B. Center-point Density Distribution in Cluster: $Lc_{i,k} > \ell_{+2.0}$



C. Center-point Density Distribution in Cluster: $Lc_{i,k} < \ell_{+2.0}$

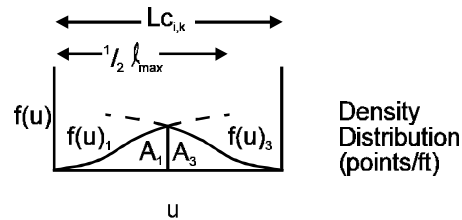
M97000700C³

Figure 3. Relationship between distribution of fracture length (part A) and average fracture center point density for long clusters (part B) and short clusters (part C). The exponential distribution of fracture center point density across the clusters (parallel to Lw) is not shown. Center point density is at a maximum, D_{zi} , in the middle of the cluster box.

And each center point is positioned away from the axis (coordinate v), on one side or the other (depending on whether R_{j2} is greater than or less than 0.5) using the following equation for an exponential distribution:

$$v_{i,j} = -m_i \ln(R_{j3}) , \quad (27)$$

where m_i is the exponential mean distance between fractures and their cluster axes. Parameters R_{j1} , R_{j2} , and R_{j3} are random numbers between zero (exclusive) and one.

The first two fractures plotted in each cluster have a slightly different plotting strategy, however. The first is plotted abutting the right or upper terminus of the cluster, and the second is plotted abutting the left or lower terminus of the cluster. Cluster geometry and fracture-plotting strategy are illustrated in Figure 4. By plotting fractures this way, the program explicitly honors the specified length distribution for clusters. A small percentage of fractures will plot outside the cluster box defined by L_c and L_w , but none will extend beyond the cluster ends unless connectivity control processes are activated.

To make fractures, each fracture center point is assigned an orientation, based either on the mean orientation and the standard deviation for the i th fracture set, or on the k th cluster's orientation and the standard deviation for the i th fracture set (if specified by setting $\theta_i = 360.0$ and assigning cluster-orientation statistics). Then, each center point is assigned a fracture length according to a user-specified distribution. Fracture length distributions are the same as for the Level 2 model, except that the default distribution has been replaced by a lognormal distribution, and the intersection frequency-controlled distribution is now defined by a lognormal mean (l_i) and a lognormal standard deviation (s_{li}). When a cluster's length is shorter than the maximum fracture length, all generated fracture lengths longer than the cluster are stored. Stored lengths are used to create the next cluster that is long enough to accommodate them. Each fracture is assigned an effective aperture from a lognormal distribution. After clusters are generated for the first fracture set, clusters are then generated for the second, third, ..., and i th fracture set.

The user of Level 4 must supply the input data file with all the variables and statistics listed in Table 4 plus the dimensions of the flow region. The generation region changes for each set and extends beyond the specified flow region by a distance equal to $l_{i,3,0} + 1/2$ times the diagonal dimension of the largest cluster in the i th set. For sets with an extremely low cluster density, the generation region expands to accommodate at least five clusters.

Connectivity Control Methods

Our approach to modeling connectivity aims to match observed T-termination frequencies, intersection frequencies (including T-terminations) and an intersection density parameter called "connectivity." "Termination" refers to the tips of fracture traces as observed on a bedding-parallel plane passing through the reservoir, and T-terminations occur where the tips appear as junctions with pre-existing fractures, regardless of the angle of intersection. Fracture traces display zero,

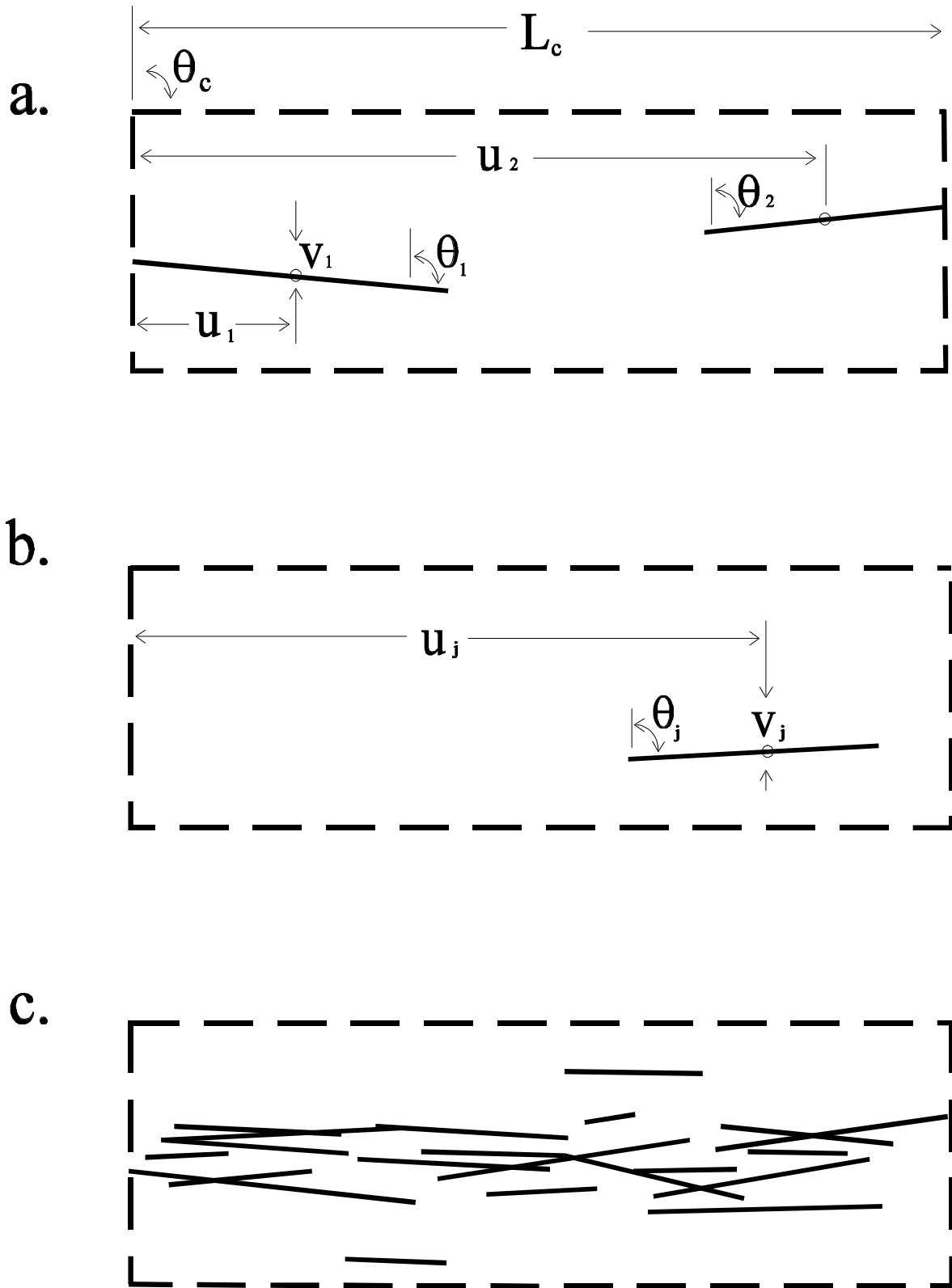


Figure 4. Scheme for plotting fractures in clusters. First and second fractures are plotted abutting the ends of the cluster box (part a). This assures correct cluster length. Fractures 3 to n are plotted randomly along the axis of the cluster (part b). Part c shows a typical cluster without connectivity control applied.

one, or two T-terminations. "Intersection" refers to any junction (fracture tips not necessarily involved) between two fracture traces, as observed on a bedding-parallel plane passing through the reservoir. "Connectivity" refers to the average number of intersections per unit fracture length (per set) and can be calculated by dividing the intersection density (the average number of intersections per unit area) by the fracture density (D_f , average trace length of fractures per unit area).

Three processes exist to control fracture intersection or termination frequencies:

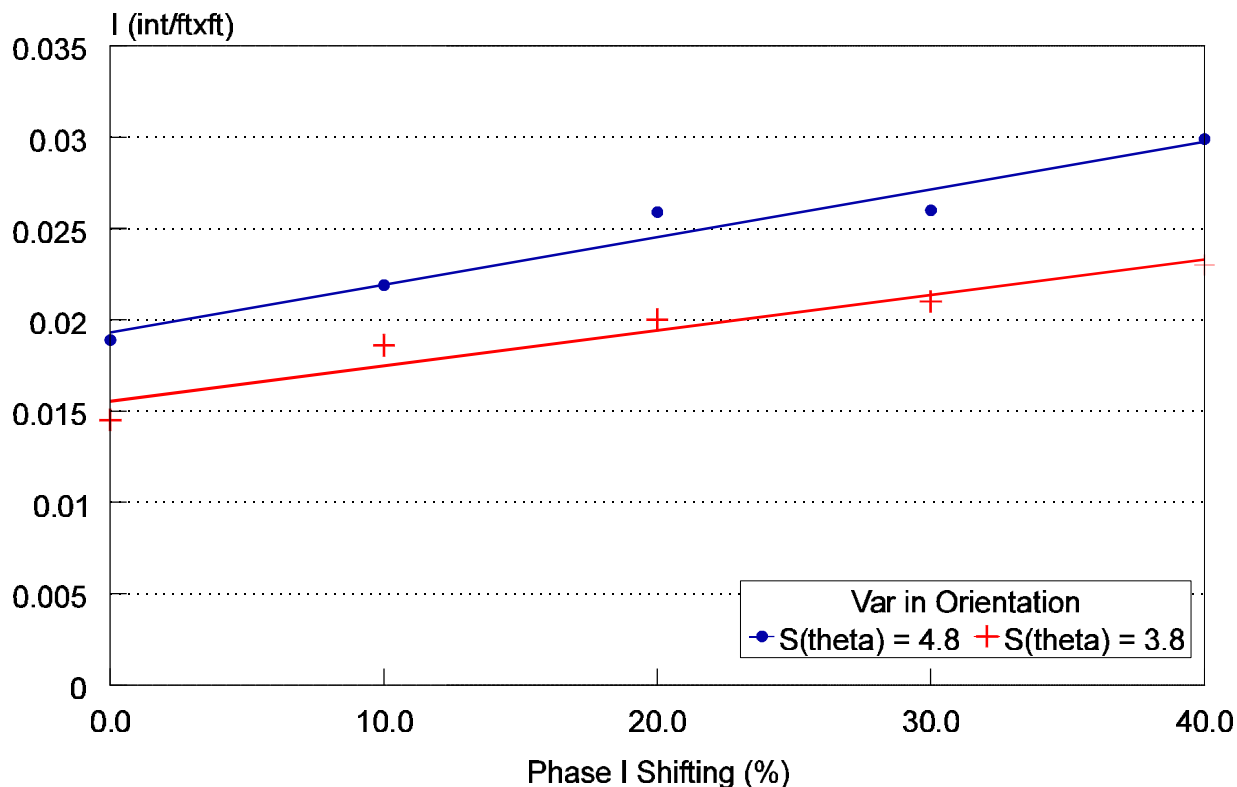
- (1) fracture end-point shifting, up to a specified percentage of fracture length;
- (2) fracture end-point shifting, coupled with synthetic annealing conditioned to specified T-termination frequencies; and
- (3) optimal fracture end-point selection, coupled with synthetic annealing conditioned to specified intersection frequencies.

The simplest process involves merely shifting each fracture end-point in either direction (toward or away from the fracture center point) to the first point of intersection found either with pre-existing fractures, or with subsequently generated fractures, or both. Shifting of the end-points to subsequently generated fractures can be limited to fractures within the same set or to fractures in subsequently generated sets. This provides a way of modeling renewed fracture growth. The maximum allowable distance for shifting is specified by the user as a percentage of fracture length. This makes intersection and termination frequency control implicit in the selection of the percentage of fracture length for which shifting is allowed (Figures 5 and 6). The maximum allowable percent shifting is usually chosen as the value that produces a target "connectivity." Fracture end-point shifting is relatively fast (because the search stops when the first intersection is found for each end), but it is inadequate to achieve the desired level of control for some projects (see, e.g., Figure 7). It can leave too many fractures unconnected to the network because, for short fractures, the percent of fracture length over which shifting can occur is small. For Levels 3 and 4, fracture end-points can be shifted beyond cluster ends.

A better technique for fracture termination control involves fracture end-point shifting coupled with synthetic annealing³ to achieve specified T-termination frequencies (see, e.g., Figure 8). In this process, a fracture is either reoriented or moved from one location to another, while also shifting the fracture end-points and counting the number of terminations produced. If the percentage of fractures having two and one T-terminations improves as a result of the effort, then the program begins to generate the next fracture; otherwise, the annealing process continues up to the user-specified limits on attribute swapping. To minimize the consequential but unintended parent-daughter clustering caused by annealing, the user will usually specify that the annealing process swap the orientation of each fracture by a maximum of two to eight times before

³FRACGEN uses a simplified synthetic annealing process. Simulated annealing refers to a conditional simulation process first used to model crystallization of molten metal. The process consists of performing a specified number of changes to independent variables (i.e., swapping fracture location or orientation) until an objective function is improved (i.e., until frequencies of T-terminations are improved). Simplification is achieved here by accepting the first set of independent variables that improves the objective function.

Intersection Density as a Function of Fracture End-Point Shifting



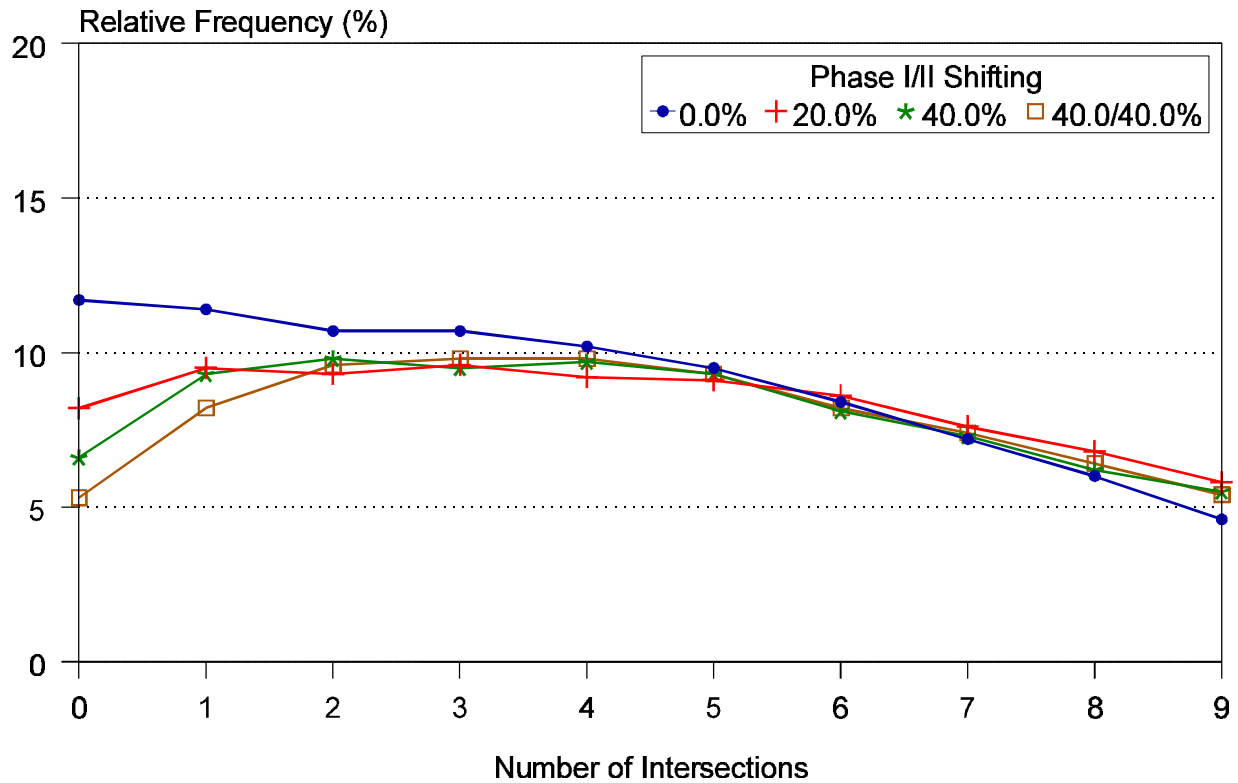
R-1 Set, MWX site

Figure 5. Intersection density (average number of intersections per unit area) increases as the maximum allowable fracture end point shifting is increased. The user generates networks with differing values of shifting and uses these resulting intersection densities or "connectivities" to select a value of shifting that produces the target intersection density or "connectivity" for the final network.

swapping the center-point location in an effort to find an acceptable number of terminations. The user may also require the generation of a specified percentage of fractures in a set before the synthetic annealing process begins. For Levels 3 and 4, a fracture may be moved only within its cluster box under the same constraints as initially imposed, but end-points may be shifted beyond the original cluster ends.

When it is more important to control the frequency of intersections than to control the frequency of T-terminations, another technique can be used to explicitly match specified intersection frequencies (see, e.g., Figure 9). With this technique, the user specifies the frequency of fractures

Intersection Frequencies as a Function of Fracture End-Point Shifting

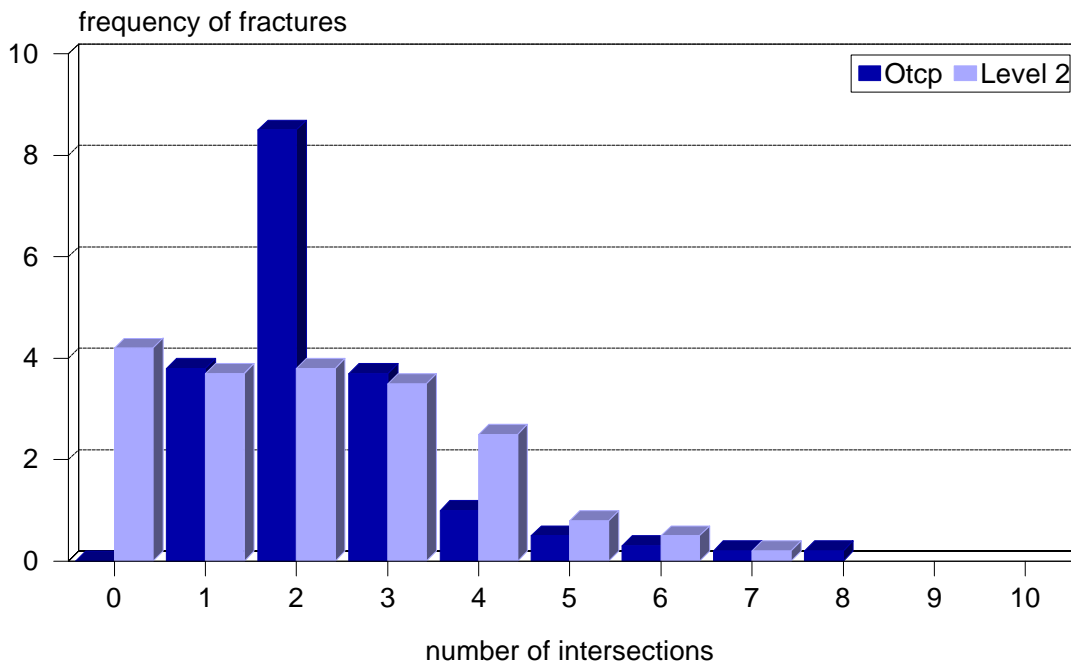


Level 1 Model

Figure 6. Fracture end point shifting significantly reduces the frequencies of fractures having zero or one intersection.

having zero to ten (or more) intersections (with T-terminations counted as intersections). A process of synthetic annealing then swaps each fracture's orientation and location, at user-specified frequencies, until a fracture can be generated that has the optimal number of intersections needed to improve the match between the generated distribution and the specified distribution of intersections. The process varies the maximum and minimum acceptable fracture lengths in an effort to match the generated length distribution with the specified length distribution, which is assumed to be lognormal. Most fractures are given two T-terminations, except those that are required to have zero or one intersection. Program efficiency is maintained by counting and optimally using all the intersections on each half of each proposed fracture of maximum acceptable length. Parent-daughter clustering is controlled as specified above. For Levels 3 and 4, a fracture may be moved only within its cluster box according to the plotting strategy for lognormal fracture lengths, but end-points may be chosen beyond the original cluster ends.

Fracture Intersection Frequencies Outcrop vs. Simulation, End-Point Shifting

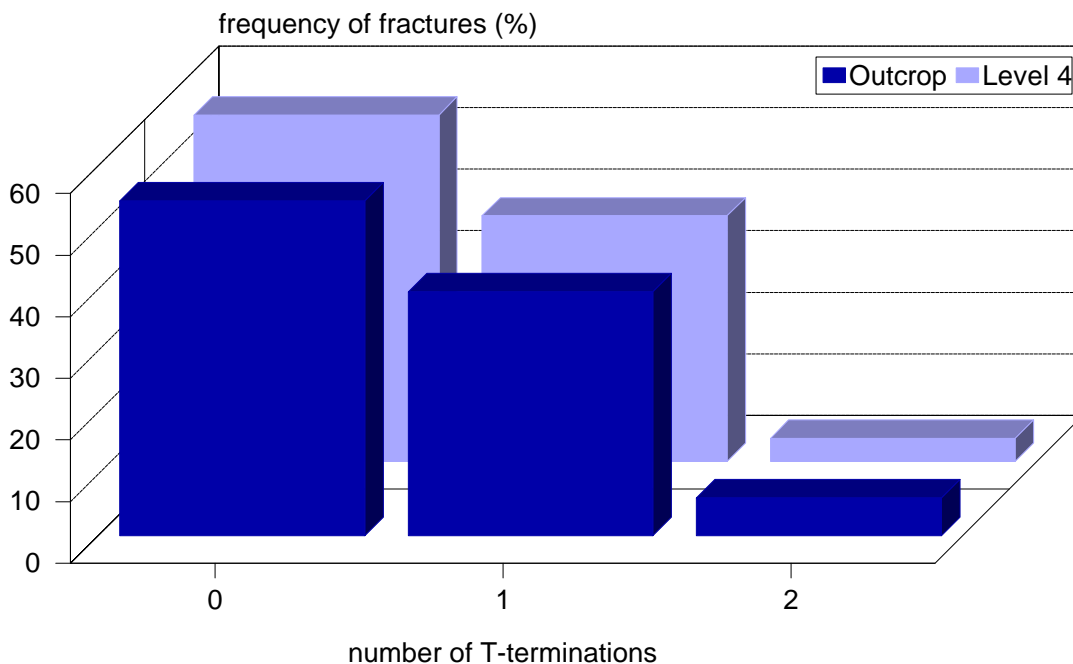


Avg. from six sample areas (20ft x 20ft)
R-2 (cross) fractures, MWX Study

Figure 7. The frequencies of cross fractures having various numbers of intersections may not match the target frequencies when only fracture end-point shifting is used for connectivity control. In this case, one of the other two connectivity control methods will provide better results (see Figure 9). In the explanation box, “Otcp” refers to “outcrop.”

This latter process is particularly useful for modeling late-formed fractures or cross-fractures, whereas the previously described technique works well for modeling early-formed or master fractures. Combined, the second and third techniques of T-termination and intersection frequency control provide a powerful means of modeling the connectivity of complex fracture networks (see, e.g., Figures 10 and 11). Usually, when fractures are relatively long, the frequency of intersections is governed primarily by the distribution of fracture lengths, so the generation process should control T-termination frequencies (assuming the distribution of fracture lengths is known from independent sources). This is accomplished with the second technique. However, when fractures are short, as with cross-fractures, fractures must be placed at optimal locations to obtain the correct intersection frequencies, given a specified nonsymmetric length distribution. The third technique does this.

T-Termination Frequencies Outcrop vs. Simulation



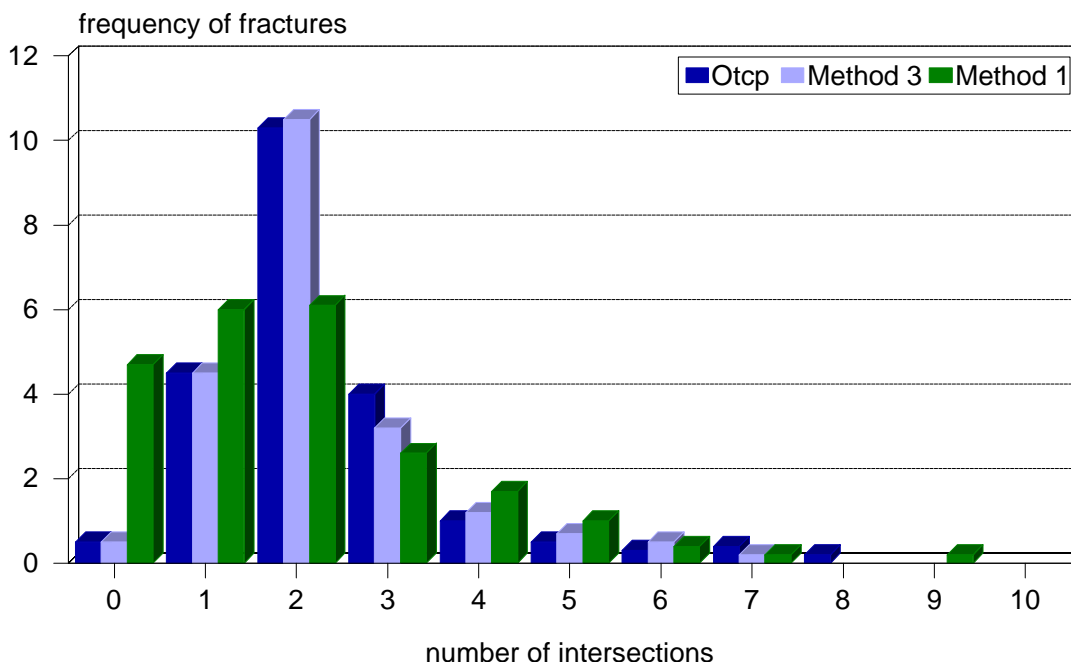
Avg. from six sample areas (20ft x 20ft)
R-1 (master) fractures, MWX study

Figure 8. T-termination frequencies of master regional fractures can be matched with target frequencies by using synthetic annealing conditioned to specified T-termination frequencies (Method 2). From a study of a Mesaverde sandstone outcrop.

After applying intersection/termination control procedures, the user should verify that the output diagnostic for "connectivity" is reasonably near the target value.

When the first two connectivity control methods are used with any fracture length distribution, the process of fracture end-point shifting skews and flattens the initial length distribution. Fracture density (D_{fi}), however, does not change because the probability of any fracture becoming longer as a result of end-point shifting equals the probability of becoming shorter by the same amount. When any of the connectivity control methods are used, fractures can extend beyond the ends of clusters where they skew and flatten the cluster length distribution.

Fracture Intersection Frequencies Outcrop vs. Simulation, Methods 1 & 3

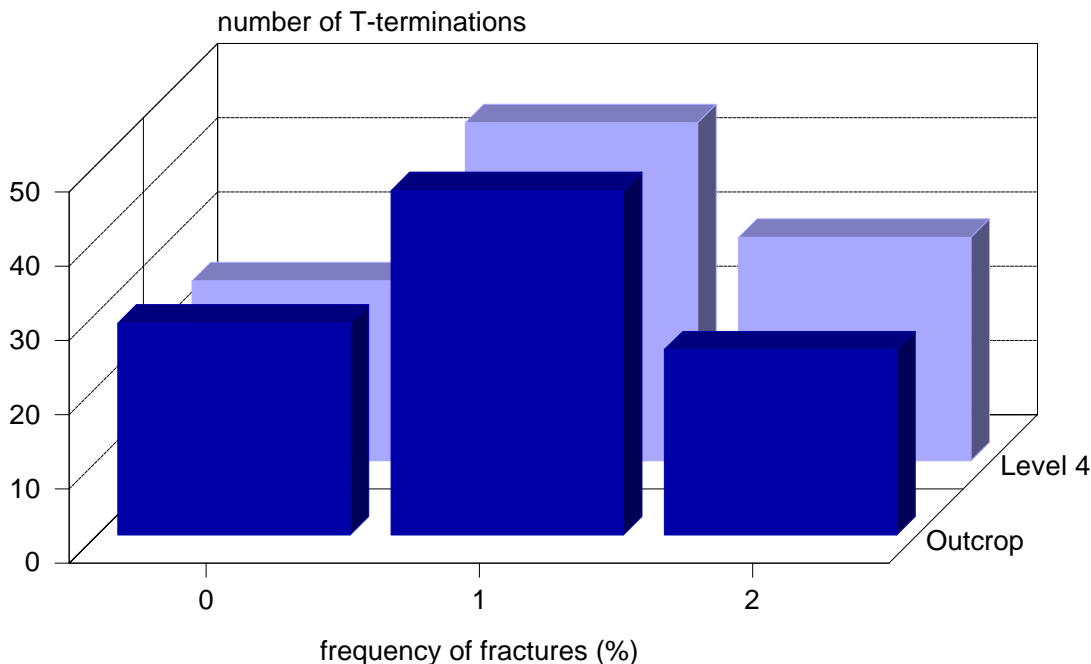


Avg. from six sample areas (20ft x 20ft)
R-2 + RR fractures, MWX Study, Level 4

Figure 9. Fracture intersection frequencies (including T-terminations) of cross fractures and late-formed random fractures can be matched with simulated annealing conditioned to specified intersection frequencies (Method 3) in cases where end point shifting alone is insufficient (Method 1). From a study of a Mesaverde sandstone outcrop.

All of the connectivity control methods generate bias in fracture locations. Alone, fracture end-point shifting generates a slight bias as fractures are moved, on average, slightly toward higher-density areas where T-terminations are more readily found. Synthetic annealing, on the other hand, is capable of extreme levels of parent-daughter clustering, which can be limited by adjusting the control parameters in the input data file. Because of the various types of bias introduced by these connectivity control methods, a user should apply these processes only after the best possible model has been generated without connectivity controls.

T-Termination Frequencies Outcrop vs. Simulation, Methods 2 & 3



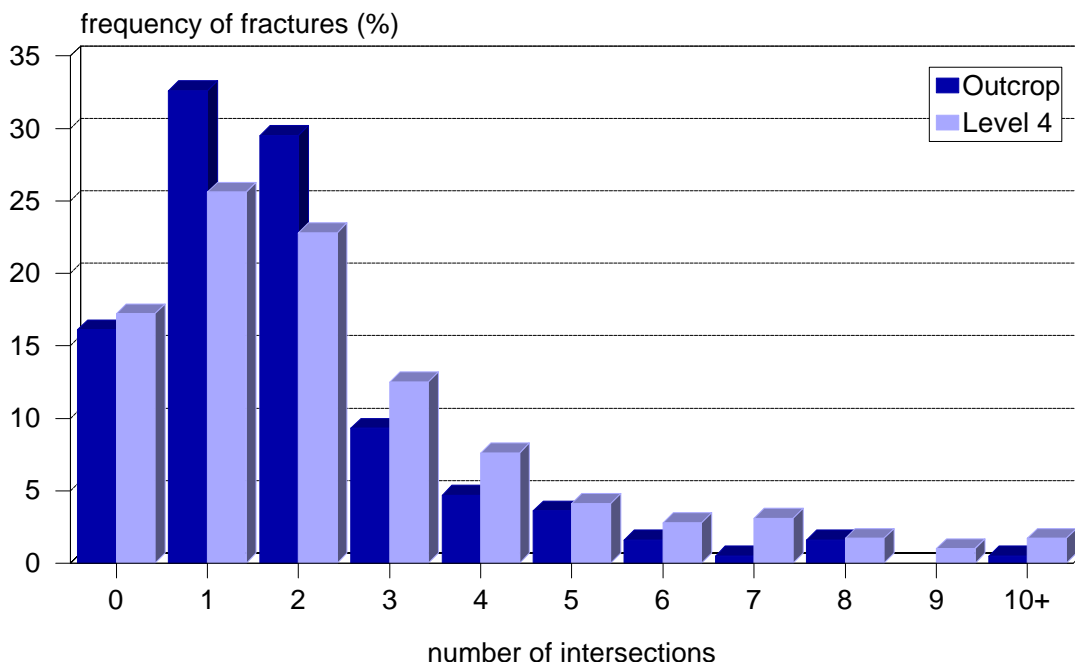
Avg. from 4 simulations (11ft x 11ft)
All Sets, Austin Chalk Outcrop

Figure 10. In our simulation of an Austin Chalk outcrop fracture pattern (see Figure 15), we used nine sets of fractures with synthetic annealing conditioned to T-termination frequencies (Method 2) to generate several early-formed sets and synthetic annealing conditioned to intersection frequencies (Method 3) to generate the other sets. End-point shifting was also used to terminate a small percentage of early-formed fractures against later-formed fractures. The aggregate result on T-termination frequencies for all nine sets is shown here.

Project Description: FRACGEN

The models described above for the fracture networks are implemented by a FORTRAN program called FRACGEN. Increasing levels of complexity in the models are part of a design to facilitate reservoir modeling. Level 1 is easy to apply, but it departs significantly from the pattern of fractures observed in most tight fractured reservoirs. Higher-level models are progressively more difficult to calibrate to a particular reservoir; however, they more accurately represent the inherent complexity of real reservoirs. The Level 1 model is particularly useful for quickly making initial

Fracture Intersection Frequencies Outcrop vs. Simulation, Methods 2 & 3



Avg. from 4 simulations (11 ft x 11 ft)
All Sets, Austin Chalk Outcrop

Figure 11. The aggregate intersection frequencies for nine fracture sets, as explained in the caption for Figure 10. The slight mismatch results from the use of connectivity control method 2, instead of method 3, for several of the sets.

estimates of the mean hydraulic aperture and the minimum area of reservoir that must be simulated. Level 2 can be used to model reservoirs in which fractures are nearly randomly located. When fractures are highly clustered, Levels 3 or 4 should be used; however, the choice of levels often depends more on the availability of data than on the anisotropy and heterogeneity of the fracture network.

FRACGEN generates fractures or clusters centered within a generation region, but it presents only the network generated within an unbiased "flow region," which is the rectangular area in which flow can be modeled. To minimize boundary effects associated with synthetic annealing, the program may reorient or relocate only fractures centered within a "buffer region," which is intermediate between the flow region and the generation region. Both the generation region and the buffer region expand to accommodate the maximum fracture length of each set; so, to minimize computing time, it is wise to employ a non-lognormal fracture length distribution that

eliminates the creation of very long fractures and minimizes the processing of large numbers of fractures in sets that include only a few long fractures.

FRACGEN reads an input file containing parameters and statistics for fracture attributes. It produces several optional outputs: a screen plot (for a VAX/VMS computer system), a plot file for making hard copies, and an output file consisting of fracture end-points and apertures (for input to the flow simulator). It also sends copious diagnostics to the screen. Diagnostics include the number of fractures touching the flow region, the "connectivity" within the flow region, the fracture density within the flow region, the numbers of fractures with zero, one, or two T-terminations within the flow region, and the numbers or relative frequencies of fractures showing zero to ten (or more) intersections within the flow region. For each set that Level 4 generates, 31 diagnostics are presented. The diagnostics allow the user to quantitatively assess the synthetic network and the functioning of the program. The diagnostics also assist the user in modeling fracture patterns observed on small outcrops or exposures where the exposure dimensions are less than the maximum fracture lengths.

Project Description: Input Data and Analysis

Input data requirements differ for the four levels of FRACGEN, and extra data are required for some of the various options that exist at each level. Most of the input describes fracture network attributes of individual sets and may be classified as either fixed variables, statistics, or percents. These input parameters are presented as symbols in Tables 1 through 5. A summary of data collection and analysis is presented below. Table 6 presents some generalized equations for calculating a few useful common statistics.

Methods of data collection and analysis also must accommodate the sources of information. Sources can be classified as one-, two- or three-dimensional. Core and borehole images give essentially one-dimensional samples of the fracture network. Most outcrops effectively provide only two-dimensional samples. Large or irregular bedding plane surfaces in outcrops should be photographed or mapped at an appropriate resolution so that the analysis can proceed on the flat image.

When a two-dimensional sample (e.g., an outcrop bedding plane) is available, the investigation should focus on a sample area. If the exposure is large, a representative sample area can be marked in the middle of the exposure so that fractures centered within the sample area do not extend beyond the boundaries of the exposure. Statistics for trace length can be determined from fractures centered within the sample area. However, when the exposure is small relative to the lengths of a significant percentage of the fractures, the investigator should collect the types of information that will match the diagnostics provided by FRACGEN for flow regions. This will permit an inverse modeling technique whereby the user selects (by trial and error) input parameters until the output diagnostics match, on average, the data that was collected on the small exposure. Scan-line samples of fracture spacing for each set will prove valuable in analyzing swarming or clustering. Scan-line samples should be taken by drawing a line perpendicular to the mean orientation of each set and recording the locations of fractures (in that set) along the scan line.

Table 6. Equations for Calculating Common Statistics	
Gaussian Distribution	$\chi = (\sum_{i=1}^n x_i)/n$ $s_x = ((\sum_{i=1}^n (x_i - \chi)^2) / (n - 1))^{1/2}$
Exponential Distribution	$\chi = (\sum_{i=1}^n x_i)/n$ $s_x = (\sum_{i=1}^n x_i)/n$
Lognormal Distribution	$\chi = \exp (U + 0.5s_u^2)$ $s_x = (\chi^2(\exp(s_u^2) - 1))^{1/2}$ $U = (\sum_{i=1}^n \ln(x_i))/n$ $s_u^2 = (\sum_{i=1}^n (\ln(x_i) - U)^2)/(n - 1)$
Uniform Distribution	$\chi = n/q$
Poisson Distribution	$\chi = n/q$ $s_x = (\sum_{i=1}^q (x_i - n/q)^2 / (q - 1))^{1/2}$
Fracture Center-Point Density	$D_i = \lambda_i / (b_i l_i \cos(\phi_i)) = \Lambda_i / (b_i l_i)$
Cluster Center-Point Density	$D_{ci} = \lambda_{ci} / (b_i l_{ci} \cos(\phi_i)) = \Lambda_{ci} / (b_i l_{ci})$
Degree of Clustering	$\zeta = 100\% (1 - n/qs^2) / (1 - n/qs_{\max}^2)$ <p>n = number of fractures of set i q = number of segments in sample line s² = variance in number of fractures per segment s_{max}² = variance if all fractures fall into one segment</p>

More often, only borehole images or cores are available. Either can be analyzed as scan-line data. Fracture length distributions and cluster length distributions remain undeterminable from these sources. Likewise, intersection and termination frequencies are undeterminable. To determine length and connectivity attributes, the investigator must turn to other sources, such as flow data, correlations between fracture length and bed thickness, outcrop analogs, and seismic data.

The most common situation facing reservoir engineers and petroleum geologists is one of limited information, primarily core or borehole imagery that show fracture locations and orientations in horizontal or inclined wells. Some information may be available from nearby analog outcrops and regional geologic studies. The approach to data collection might follow a path similar to the one we used at the Multi-Well Experiment (MWX) site, as follows. First, the investigator reviews the regional geology for basic information that could help with the interpretation of observations in the borehole and at nearby analog outcrops. Fracture network attributes are predicted. Next, from borehole images or core, the investigator obtains data on fracture orientation, which are used to define observed sets in the target reservoir. The linear density of fractures (i.e., the average number of fractures encountered per unit length of sample line that is oriented normal to the fracture set = Λ_i) is calculated for each set observed in the borehole.

This linear density is then compared to the linear density of a similar set in an analog outcrop after adjusting for differences in bed thickness and any other significant correlatable parameters. The goal is to estimate fracture length statistics for the reservoir. An assumption is usually made that any excess (unaccounted) linear density observed in the outcrop results from extra fracturing caused by unloading and weathering. If the excess linear density results from short fractures forming between the longer fractures to relieve local stresses, the investigator may discard data on all (or most) of the short fractures that are not needed to gain a match with the observed linear density of the target reservoir. From the retained subpopulation of longer fracture traces in the outcrop, the investigator estimates the fracture length statistics. Methods of correction have been published by several authors for various types of bias and censoring.

Cluster lengths are much more difficult to estimate. But some progress may be made by studying large analog outcrops, detailed structure maps, high-resolution seismic imagery, and well interference data. The investigator may need to extrapolate between small-scale fracture swarms, which are measurable in outcrops, and large-scale fracture swarms, which are observable on seismic imagery or interpreted from other sources. Otherwise, the investigator may have to start the modeling process assuming short clusters and gradually increase cluster length (holding cluster density constant) until suitable flow simulations are achieved. Whatever the case, the user of FRACGEN should keep clusters as short as practical to minimize computer processing time and memory.

Given the fracture sets, fracture orientation statistics, fracture length statistics, and an estimate of cluster length statistics, the investigator can calculate the other required input parameters. Taking this approach, the Level 4 (lognormal fracture length) calculations are summarized in Figure 12. When analyzing borehole or core data, fracture sets might be defined solely on orientation. Modes in histograms of orientation measurements are interpreted as sets, and all the fractures are assigned to the mode-based sets or to a randomly oriented set. But when two-dimensional exposures are analyzed, other fracture attributes are considered in defining sets. Sometimes, more

Figure 12. Simple Approach to Input Data Analysis**from well logs:**

fracture orientation (θ_i , $s_{\theta i}$, $b_i=f(s_{\theta i})$)

linear density of fractures (Λ_i)

from analogue outcrops:

fracture length (l_i , s_{li})

cluster length (l_{ci} , s_{lci})

calculate:

mean exponential spacing (m_i)

$$m_i = m_i^* / (10 \Lambda_i)$$

fracture density (D_{fi})

$$D_{fi} = \Lambda_i / b_i$$

intra-cluster fracture density

$$d_i = D_{zi} = v_i n_i^* / (12 m_i l_i b_i \cos(\phi_i))$$

$$s_{di} = 0.0$$

cluster density (D_{ci})

$$D_{ci} = D_{fi} / [12 m_i (l_{ci} - l_{i,2.0} + \kappa_{i,1} (l_{i,2.0} - l_{i,3.0})) d_i l_i]$$

where

$\kappa_{i,1}$, v_i , b_i = correction factors (explained in text).

ϕ_i = angle between pole to fracture set and scanline sample.

$l_{i,2.0}$ = fracture length at 2.0 standard deviations.

than one set can be found to occupy a mode in the histogram of orientation. For purposes of modeling, the investigator should pay attention to termination frequencies, which help to discriminate sets and to ascertain their relative ages. Sets should be modeled in chronological order to help generate appropriate hierarchial relations.

The process of analyzing clusters from well bore or scan-line data is illustrated in Figure 13. In many reservoirs, fractures are obviously grouped into clusters or swarms. Each fracture set observed along a borehole has swarms at locations ostensibly independent of other fracture swarms of the same set and other sets. The number of fractures intersected per swarm may vary from one fracture to tens of fractures. A person might expect to subjectively group fractures into clusters, but our studies of fractures intersecting the RET #1 well showed that fractures could be grouped into large, small, or intermediate-sized clusters, or they could be grouped into variable-sized clusters, without any certainty as to which groupings represent real fracture swarms. Determining what constitutes real clusters in a scan-line sample is further complicated in that clusters theoretically could merge, overlap, or have smaller clusters within them (i.e., large-scale spatial correlation). Moreover, given a small sample space, even random placement of fractures leads to a chance of apparent clustering. And, if a Poisson process is used to generate synthetic clusters, a subjective data analysis will not account for the overlapping clusters produced by the model.

To aid in analyzing clustered events sampled along a scan line, a computer program was written to generate a one-dimensional sample of the Level 3 model of a clustered fracture set. Using this program, several families of cumulative frequency curves were generated for selected values of m_i (exponential mean distance between fractures and their cluster axis) and n_i (average numbers of fractures intersected per cluster) (see, e.g., Figure 13, No.3). The investigator compares these theoretical curves with the normalized cumulative frequency distributions of fracture spacing observed along the sample line (normalized to 10-unit spacing, average; see, e.g., Figure 13, No. 2). From this comparison, the investigator estimates the observed distribution's values for the average number of fractures per cluster intersected by a sample line (n_i^*) and the normalized exponential mean distance between fractures and their cluster axis (m_i^*). A computer program called SPA.BAS calculates the normalized cumulative frequency distribution for fracture spacing.

The analytic technique just presented is designed for the Level 3 model and is applicable to the Level 4 model when the standard deviation of intracluster fracture density is zero ($s_{di} = 0$). A good technique for estimating s_{di} has not yet been developed. A biased estimate of s_{di} may be made by subjectively analyzing the individual clusters penetrated by the sample line. The key to this approach is to properly assign fractures to clusters so that an accurate count of the fractures per cluster ($n_{i,k}$) is obtained. The n_i^* and m_i^* values estimated from the normalized cumulative frequency distribution will help in making plausible assignments of fractures to clusters. The previously estimated m_i^* value (divided by $10\Lambda_i$) should roughly equal the m_i parameter calculated in this technique. When this technique of analyzing clusters is applied, the calculations differ slightly for Level 3 and Level 4 applications.

For Level 4, the user must apply the equation separately to the $n_{i,k}$ values for each cluster penetrated by the sample line:

$$D_{zi,k} = v_i n_{i,k} / (12 m_i l_i b_i \cos(\phi_i)) , \quad (27)$$

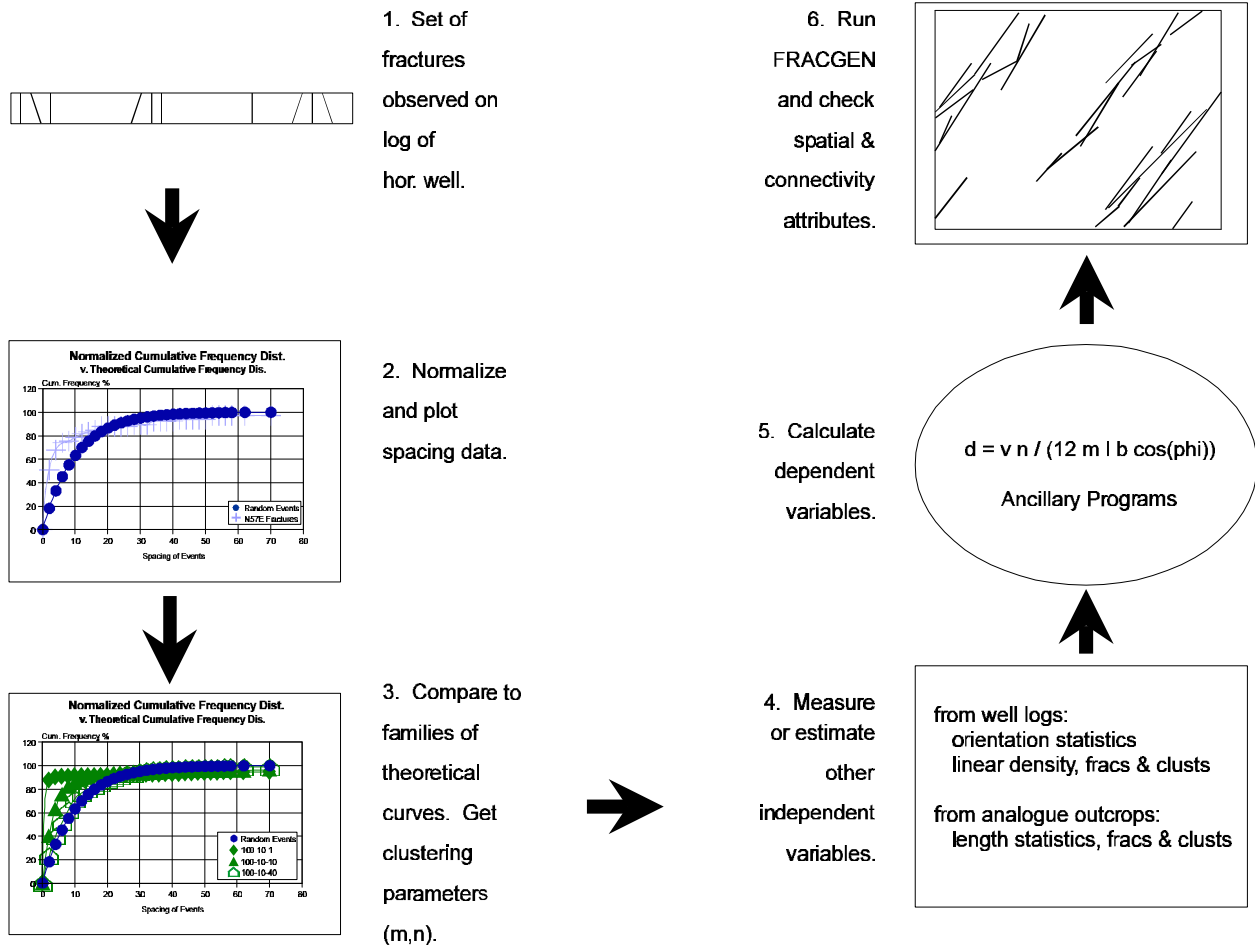


Figure 13. The six main steps to modeling clusters. Fracture spacing observed in a bore hole or scan line sample (1) is normalized and plotted in a cumulative frequency curve (2) for comparison with theoretical curves (3). The investigator can then estimate m_i^* (the average distance between fractures and their cluster axis) and n_i^* (the mean number of fractures per cluster intersected by the sample line). These values, along with estimates of other key parameters (4) taken from other sources, are used to calculate the remaining input parameters.

where

$D_{zi,k}$ = an estimate of the intracluster fracture center-point density of the k th cluster in the i th set,

$n_{i,k}$ = the number of fractures in the k th cluster, and

ϕ_i = angle between pole to fracture set and scanline sample.

The arithmetic average distance between fractures and their cluster axis for set i is

$$m_i = [(\sum_{k=1}^q \sum_{j=1}^n |m_{i,k,j}|) / \sum_{k=1}^q n_{i,k}] \cos(\phi_i) \approx m_i^*/10\Lambda_i, \quad (28)$$

where

q = number of clusters sampled, and
 n = total number of fractures in the sample.

Variance in fracture orientation for set i , assuming vertical fractures, may be accounted for with

$$b_i = \int_{\theta_{\min}}^{\theta_{\max}} \cos(\theta) p(\theta) d\theta, \quad (29)$$

which is implemented in a computer program called BCALC.BAS.

And, a correction for the risk of sampling near cluster ends, where fracture density is lower, may be estimated with equations that account for the mean cluster length, l_{ci} , relative to the maximum fracture length, $l_{i,max}$, as follows.

$$v_i = 1 / [1 + 2(\gamma - 1)(l_{i,max} / l_{ci})] \quad (30)$$

The parameter v_i includes a γ value that approximates the fraction (or weight) that upon multiplication with the maximum intracluster fracture density of the k th cluster ($l_i d_{i,k}$) gives the weighted average intracluster fracture density (ft/ft²) in the regions of reduced density at each end of a cluster.

$$\gamma = \overline{D_{fci}(x)} / D_{fci} \text{ for all } x \leq l_{\max} \text{ along the axis of a cluster.} \quad (31)$$

To calculate γ , a relation is needed to express intracluster fracture density, $D_{fci}(x)$, at any location x along a cluster axis. The concept is that the fracture density contributed by fractures of length l at any location x is a product of the number (or fraction) of fractures of length l times length l divided by the area within the cluster where the center points may be plotted. This quantity must be multiplied by the fractional area where the fracture center points can be plotted to contribute to the fracture density observed at location x . We currently calculate γ with a computer program, called CLUSDEN.BAS, that implements a summation process assuming either a discrete fracture length distribution or a discretized fracture length distribution. The basic calculations may be generalized for any continuous fracture length distribution ($p(l)$) as follows (subscripts for set i omitted).

$$D_{fc}(x) = \int_{l_{\min}}^x \frac{p(l) l}{L_w (l_c - l)} dl + \int_x^{l_{\max}} \frac{p(l) x}{L_w (l_c - l)} dl, \text{ for } (l_c - l) \geq x \quad (32)$$

and

$$D_{fc}(x) = \int_{l_{\min}}^x \frac{p(l) l}{L_w (l_c - l)} dl + \int_x^{l_c - x} \frac{p(l)x}{L_w (l_c - l)} dl + \int_{l_c - x}^{l_{\max}} \frac{p(l)}{L_w} dl, \text{ for } (l_c - l) < x . \quad (33)$$

Intracuster fracture density near the middle of long clusters, where end effects do not exist, may be calculated with

$$D_{fc} = \int_{l_{\min}}^{l_{\max}} \frac{p(l) l}{L_w (l_c - l)} dl , \text{ for } l_{\max} \leq x \leq (l_c - l_{\max}) . \quad (34)$$

All other variables are defined elsewhere (see Tables 3 & 5).

The Level 4 intracuster fracture density parameters, d_i and s_{di} , are estimated as the lognormal mean and standard deviation of the $D_{zi,k}$ values. Because the Level 4 technique of analyzing clusters (Equation 27) does not explicitly account for the probability of cluster overlap and the other problems of cluster recognition (described above), this technique usually overestimates the d_i and s_{di} values.

For Level 3, an equation is applied to the lognormal mean of the $n_{i,k}$ values:

$$D_{zi} = v_i n_i / (12 m_i l_i b_i \cos(\phi_i)) , \quad (35)$$

where

n_i = lognormal mean of $n_{i,k}$ values $\approx n_i^*$,
 m_i = Eq. 28,
 b_i = Eq. 29, and
 v_i = as defined above.

In applying equations 27 through 35, we assume that all clusters are manifest by at least one fracture per cluster intersecting the sample line. Where there are only a few short unconnected fractures making a cluster, there is the possibility of under-sampling caused by a sample line passing through the cluster without touching any fractures. We have not developed a solution for this problem.

When comparing fracture density for different data sets or for the same data set modeled by different levels of the computer program, the investigator should compare the two-dimensional fracture density, D_f . Two-dimensional fracture density refers to the total length of fracture traces (lines) in a representative area and has units of ft/ft². Such density has the following relationships.

For Level 1,

$$D_f = l D. \quad (36)$$

For Levels 2, 3 and 4,

$$D_f = \sum D_{fi}, \quad (37)$$

where for Level 2,

$$D_{fi} = l_i D_i ; \quad (38)$$

for Level 3 and 4 nonskewed fracture length distributions,

$$D_{fi} = 12 m_i (l_{ci} - l_i) D_{zi} l_i D_{ci} ; \quad (39)$$

and for Level 3 and 4 skewed fracture length distributions

$$D_{fi} = 12 m_i (l_{ci} - l_{i,2.0} + \kappa (l_{i,2.0} - l_{i,-3.0})) d_i l_i D_{ci} , \quad (40)$$

where

$$\kappa = Eq. 18 . \quad (41)$$

For nonskewed length distributions (continuous uniform, discrete uniform, and continuous nonuniform),

$$l = (l_{\max} + l_{\min}) / 2 , \quad (42)$$

$$l_i = (l_{i,\max} + l_{i,\min}) / 2 , \text{ and} \quad (43)$$

$$l_{ci} = (l_{ci,\max} + l_{ci,\min}) / 2 . \quad (44)$$

And, for skewed length distributions (including intersection frequency controlled),

$$l_i = \exp (U_{li} + 0.5 s_{uli}^2) \quad (45)$$

and

$$l_{ci} = \exp (U_{lci} + 0.5 s_{ulci}^2) . \quad (46)$$

All other parameters are previously defined (see also Table 5).

Results: Example Output, Verification/Validation, Speed

We have conducted studies of: (1) a fractured Devonian shale reservoir penetrated by the U.S. DOE's RET #1 well in Wayne County, West Virginia; (2) the fractured paludal sandstones penetrated by the U.S. DOE's Multi-Well Experiment (MWX) wells near Rifle, Colorado; (3) a Mesaverde sandstone outcrop fracture pattern mapped near Rifle, Colorado (from Lorenz and Finley, 1991); and (4) an Austin Chalk outcrop fracture pattern mapped in a quarry near San Antonio, Texas (from Corbett and others, 1991). These case studies have provided “lessons-learned” for incremental development of the software and have demonstrated that the software is capable of modelling complex fracture patterns.

We have conducted several input data analyses to verify that the chosen distributions for input variables sufficiently match reality. Goodness-of-fit tests were applied to data collected from a Mesaverde sandstone outcrop near Rifle, Colorado and from MWX site cores. The sandstone outcrop contained an early-formed regional fracture set, a later-formed cross-fracture set, and a few random fractures. We found that for all three sets, fracture placement could be adequately modeled with random placement of fracture center-points. Fracture orientation could be adequately represented with Gaussian distributions (two orthogonal sets with large standard deviations were used to produce the random set). Fracture trace lengths could be adequately modeled with lognormal distributions. And, fracture intersection and termination frequencies could be closely matched through synthetic annealing processes.

Hydraulic fracture apertures could not be tested for lognormality, but the reported gross apertures in MWX core (Finley and Lorenz, 1988) are not obviously non-lognormal. The most significant departure from the theoretical distributions used in FRACGEN was found for fracture height, as reported for the MWX core (Finley and Lorenz, 1988). Instead of a fixed fracture height equal to the thickness of the bed, fracture height may be independent of bed thickness when the thickness is more than a particular (but undetermined) value or when the reservoir contains small lithologic discontinuities (e.g., shale partings) (see Lorenz et al., 1989). Parameters for clustering could not be tested at this site because the fractures have nearly random center-point locations. However, for the RET #1 well data, the one-parameter exponential distribution (of distance between fractures and their cluster axis) did fit a fracture set that was tested.

Figure 14a is a sample synthetic fracture network generated from the Mesaverde sandstone fracture map. Figure 14b shows a portion of the fracture map at the same scale for comparison. Similarly, Figure 15a is a sample synthetic fracture network generated from the Austin Chalk fracture map, and Figure 15b shows, for comparison, a straight-line tracing of a portion of the fracture map. Comparisons of T-termination frequencies and intersection frequencies are shown in Figures 8 and 9 for a Mesaverde sandstone and in Figures 10 and 11 for the Austin Chalk. To illustrate FRACGEN's ability to model clustering, a realization of one set of fractures observed in the RET #1 borehole video is presented as Figure 16.

Computer speed varies primarily as a function of the termination/intersection control processes and as a function of maximum fracture lengths and maximum cluster lengths. On a Pentium 200-equivalent computer, FRACGEN requires from several seconds to a few minutes to generate typical networks without termination/intersection control. With fracture end-point shifting in effect, the run time increases as a function of the number of fractures generated and the fracture length distributions. With synthetic annealing also in effect, the run time further increases as a function of the number of swaps. The realization in Figure 20 required 8 minutes, and the realization in Figure 14 required 21 minutes.

Reservoir Flow Simulation

Objectives: Drainage of Complex Fracture Network and Matrix

The mathematical model described below was developed to study reservoir performance as a function of fracture pattern, fracture network connectivity, and variations in matrix block size populations and locations. To this end, the model characterizes the reservoir in terms of the fluid carrying capacity of fractures, fluid flow paths, and the effective volumes drained by fracture segments.

Approach: Mathematical/Numerical Model

The material balance and flow equations that constitute the mathematical model for the gas reservoir simulator are developed in the following way. The reservoir is represented by a collection of flow paths that intersect at points referred to as nodes. The flow paths consist of both the fracture network and the horizontal wells. Each flow path is subdivided into segments by the nodes. Each segment is recharged by gas from the surrounding matrix rock. In the model, the recharge flow is lumped at the midpoint of each segment (Figure 17). The recharge flow to each segment is modeled by two one-dimensional systems that represent the dynamics of flow in the matrix rock on either side of the path. Each of these systems is assigned an effective volume based on the network geometry. The nodes formed by the intersection of two fractures are called normal nodes, while nodes formed by the intersection of a well and the fracture network are called well nodes.

Fracture Network

MWX4A.GRF

FRACTURE WIDTHS

0.0000500

FLOW REGION

75.0 X 75.0

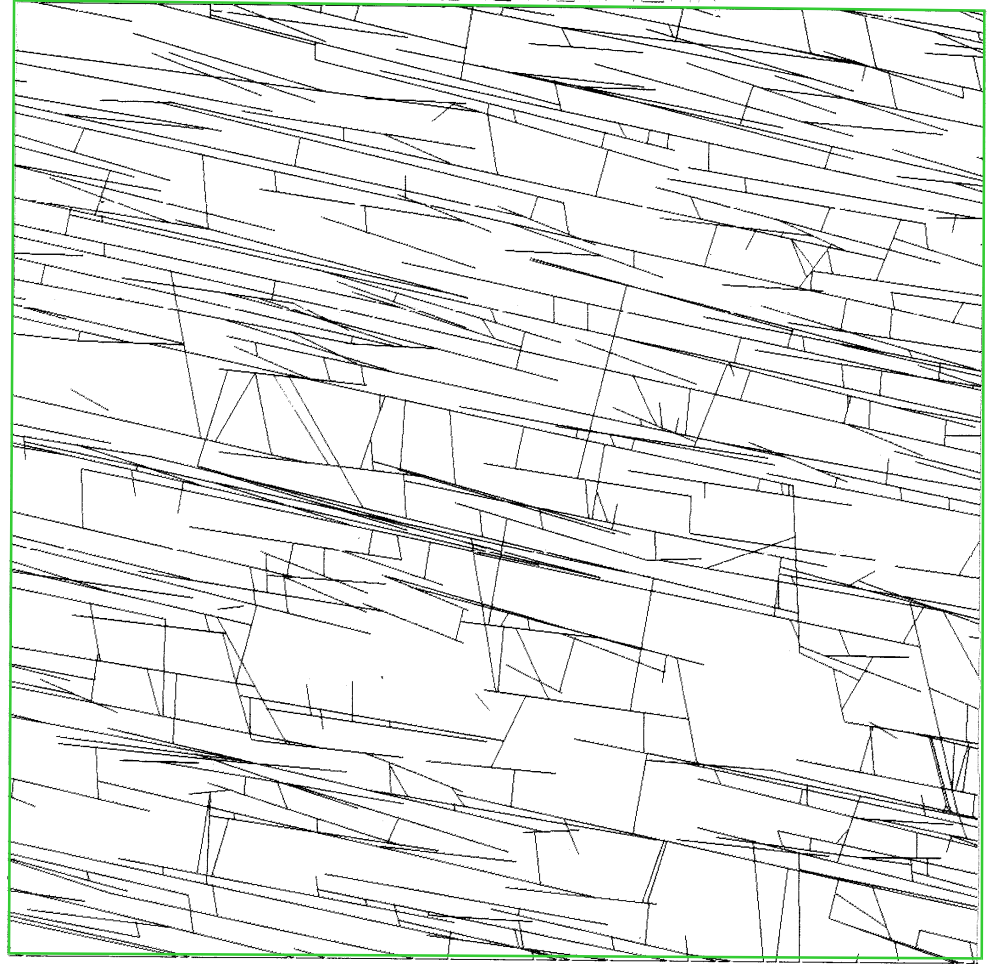
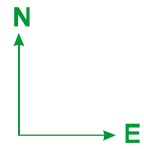


Figure 14a. This realization was generated using data from the Mesaverde sandstone outcrop fracture map (see Figure 14b). T-termination frequencies were explicitly controlled on the master fracture set. Intersection frequencies were explicitly controlled on the cross fractures and random fractures.

Normal nodes are simply summing points. The model equation for a normal node is obtained by requiring that the molar inflows to that node sum to zero. The following notation is used for the model description (see Figure 18). The normal node for which a material balance is being written is labelled P and the four segments (and their corresponding mid-points) that meet at that node are labelled e, w, n, and s with the nodes at the other ends of the segments labelled E, W, N, and S respectively. The volumetric flow rate in the fractures is modeled using the expression

$$Q_v = - \frac{hw^3}{12\mu} \frac{dp}{ds} \quad (47)$$

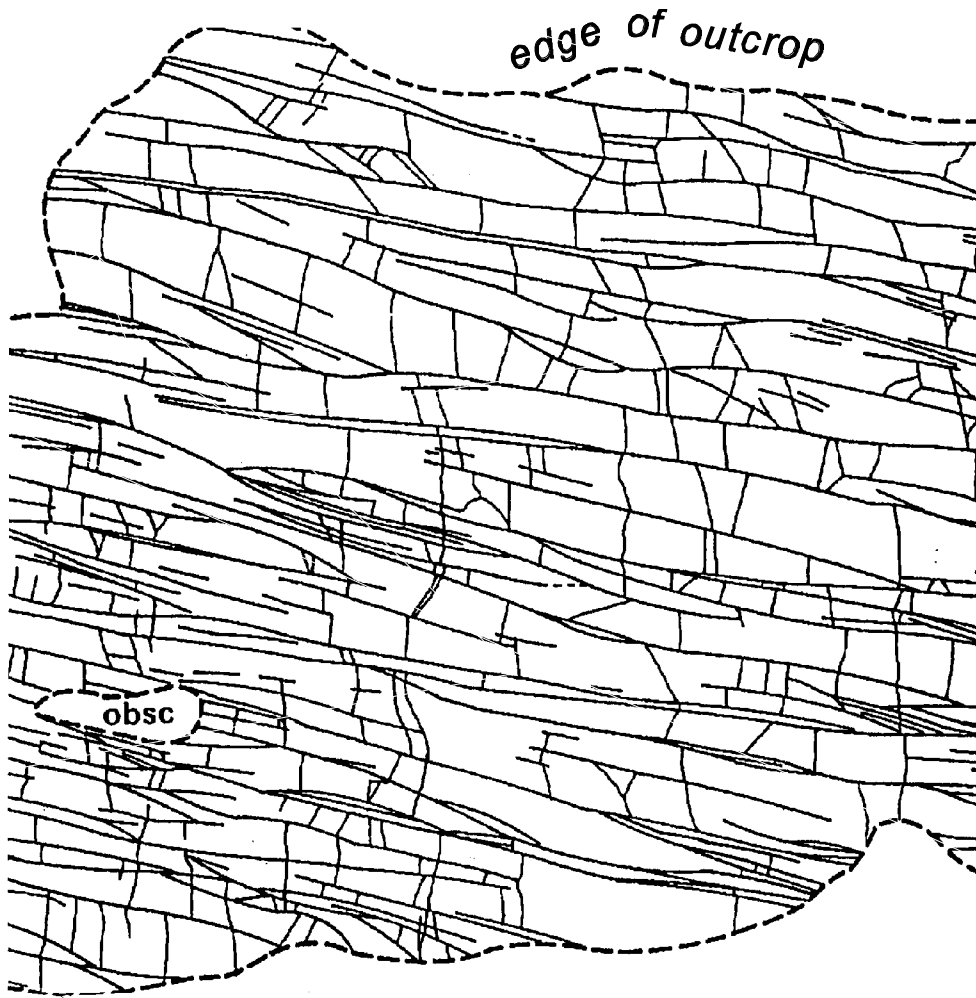


Figure 14b. This is a portion of the Mesaverde sandstone outcrop fracture map presented by Lorenz and Finley, 1991 (reprinted by permission of the American Association of Petroleum Geologists and Datapages, Inc.). It is at the same scale as the realization in Figure 14a.

where h is the formation thickness, w is the fracture aperture, μ is the gas viscosity, and $\frac{dp}{ds}$ is the gas pressure gradient. The molar gas density is given by the real gas equation of state

$$\rho = \frac{1}{RT} \frac{p}{Z} \quad (48)$$

Fracture Network

ALAMO2a.GRF

FRACTURE WIDTHS

0.0000700

FLOW REGION

11.0 X 11.0

N
E

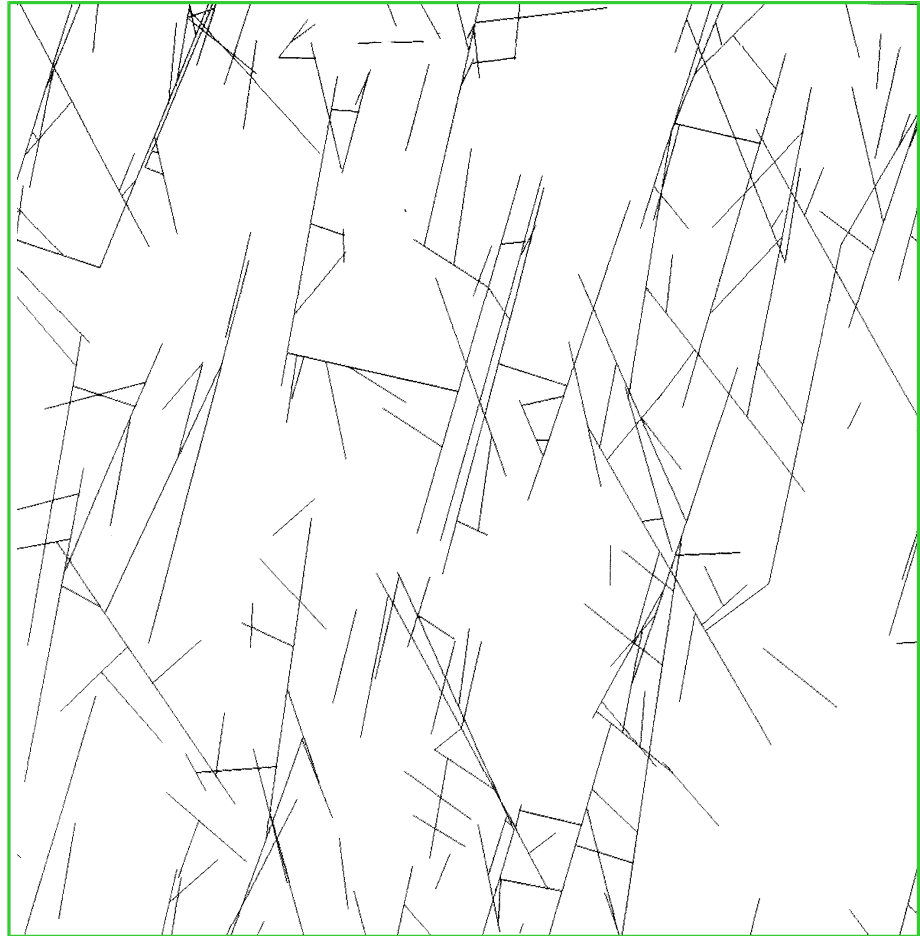


Figure 15a. This realization was generated using data from the Austin Chalk outcrop fracture map (see Figure 15b). Termination frequencies were explicitly controlled for early formed sets in this realization, and intersection frequencies were explicitly controlled for later-formed sets. End point shifting was used to connect a few early formed fractures to later-formed fractures.

where R is the gas constant, T is the temperature, and Z is the Z factor which is a function of T and p . The reservoir is assumed to be isothermal so the temperature dependence of Z is suppressed in the derivation. Writing the material balance at P yields

$$\begin{aligned}
 & - \left(\frac{hw^3}{12\mu} \right)_w \left(\frac{1}{RTZ} \frac{p}{ds} \frac{dp}{ds} \right)_{P-w} + \left(\frac{hw^3}{12\mu} \right)_e \left(\frac{1}{RTZ} \frac{p}{ds} \frac{dp}{ds} \right)_{P-e} \\
 & - \left(\frac{hw^3}{12\mu} \right)_s \left(\frac{1}{RTZ} \frac{p}{ds} \frac{dp}{ds} \right)_{P-s} + \left(\frac{hw^3}{12\mu} \right)_n \left(\frac{1}{RTZ} \frac{p}{ds} \frac{dp}{ds} \right)_{P-n} = 0 \quad .
 \end{aligned} \tag{49}$$

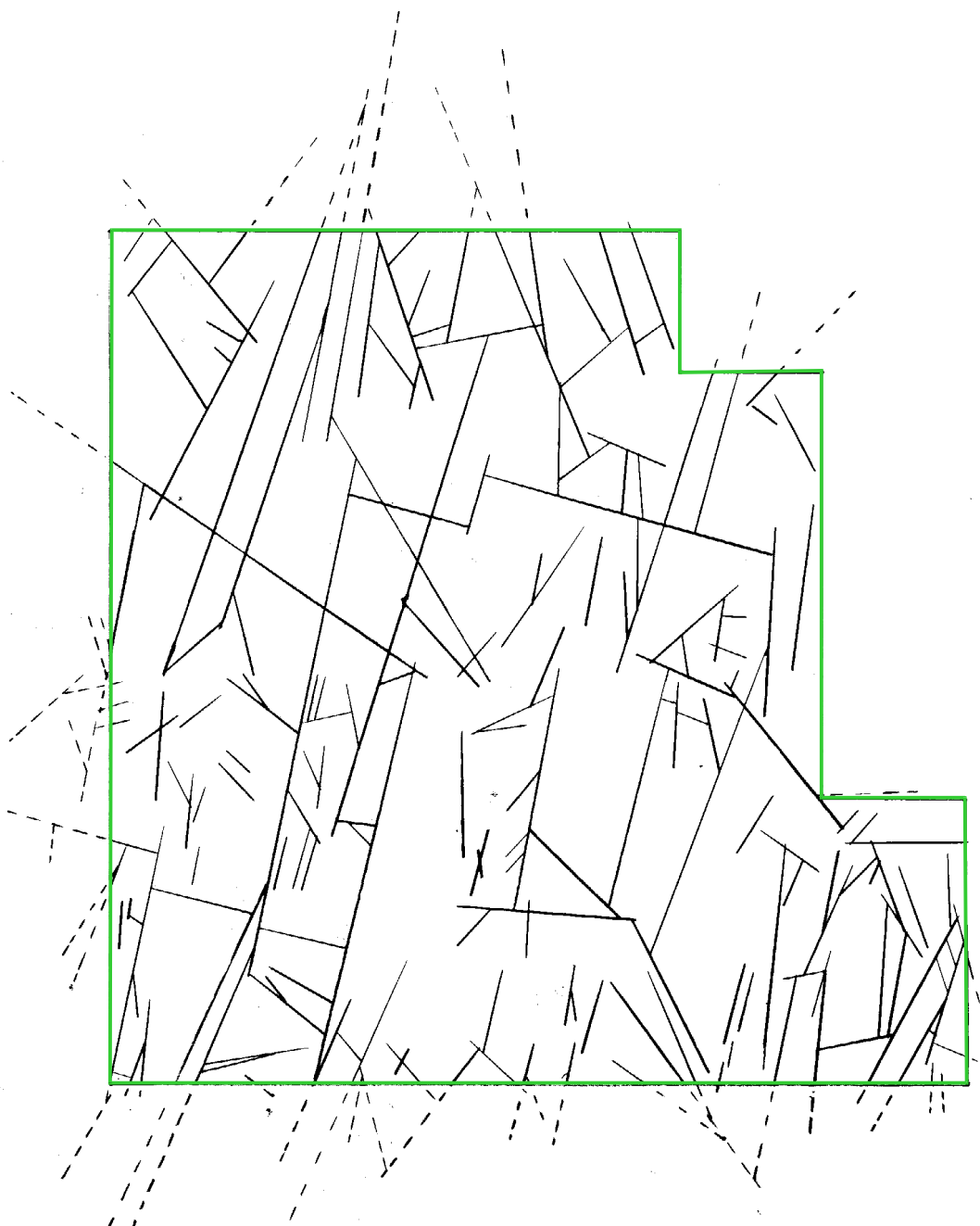


Figure 15b. Straight line tracing of the rather sinuous fractures mapped by Corbett et al., 1991, (Dallas Geological Society Field Trip Guidebook #4, p. 27) in a quarry of the Austin Chalk. According to Corbett et al., "[a] large portion of the fractures are altered or filled and isolated from other fractures." This pattern represents the typical pattern that occurs between the significant fault and fracture zones, which make productive wells. Flow between the significant fault/fracture zones is minimal and slow. Flow simulations on synthetic realizations of this pattern might be used to help determine permeability tensors of "matrix" between the main fracture zones for a larger simulation of the reservoir.

Fracture Network

RET4B.GRF

FRACTURE WIDTHS

0.0000500

FLOW REGION

500.0 X 500.0



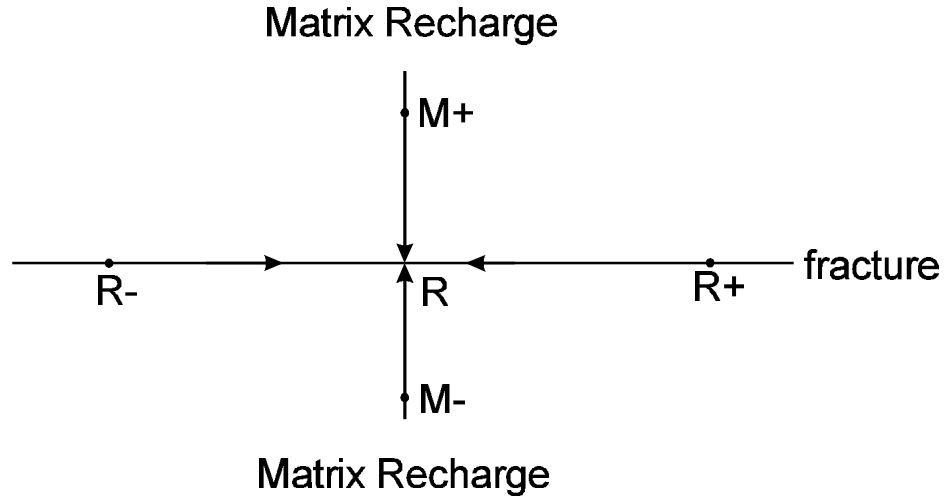
M97000882 C3

Figure 16. This figure illustrates clustering produced by FRACGEN. It shows one set (or subset) of fractures as observed by Overbey et al. (1987) in the well bore video of the RET #1 well that was drilled into the Devonian shale in Wayne County, West Virginia. These fractures are highly clustered. The reservoir contains several other sets that are not shown on this illustration.

By defining the real-gas pseudopotential (potential for short) as

$$\Phi = \int_0^p \frac{p' dp'}{\mu(p') Z(p')} , \quad (50)$$

Material Balance at Recharge Points



$$2T_R^f (\Phi_R^f - \Phi_R^f) + 2T_R^f (\Phi_R^f - \Phi_R^f) + T^m (\Phi^m - \Phi_R^f) + T^m (\Phi^m - \Phi_R^f) = 0$$

M97000884 C3

Figure 17. Each fracture segment is recharged at its midpoint by the matrix on both sides of the fracture. T intersections are treated as non-terminal intersections with the terminating fracture extending a very short distance into the matrix block on the other side. Gas pressure in the fracture segment establishes the unsteady boundary condition for modeling flow into the fracture segment. Therefore, recharge of the fracture segment is determined, in part, by the pressure history in the segment.

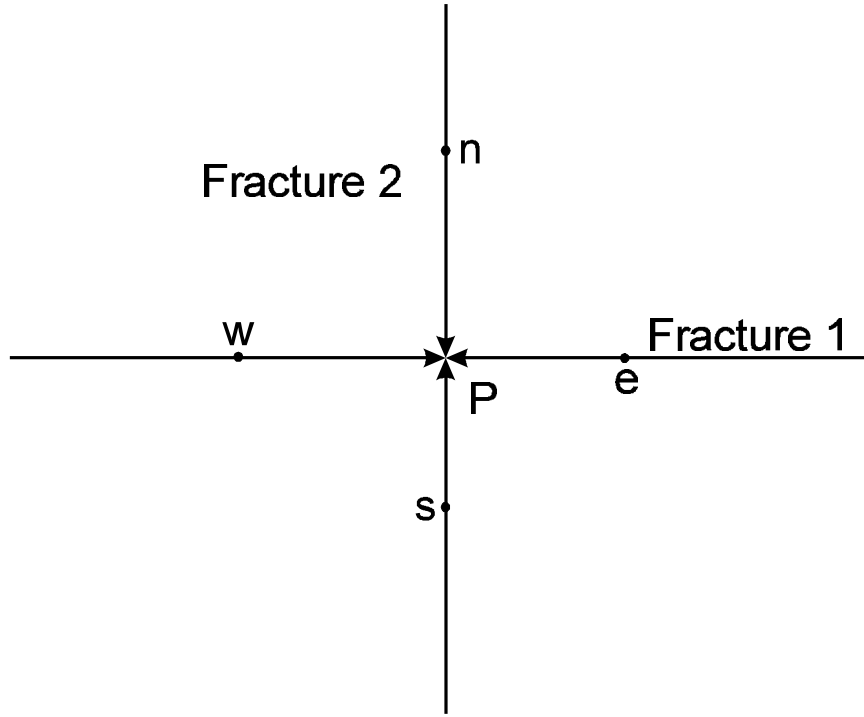
Equation 49 can be rewritten as

$$-\left(\frac{hw^3}{12}\right)_w \left(\frac{d\Phi}{ds}\right)_{P-w} + \left(\frac{hw^3}{12}\right)_e \left(\frac{d\Phi}{ds}\right)_{P-e} - \left(\frac{hw^3}{12}\right)_s \left(\frac{d\Phi}{ds}\right)_{P-s} + \left(\frac{hw^3}{12}\right)_n \left(\frac{d\Phi}{ds}\right)_{P-n} = 0 \quad (51)$$

Since fluid enters the flow paths only at the recharge points, the molar flow is a constant between a recharge point and a node, thus Equation 51 can be expressed without further approximation by

$$\begin{aligned} & -\left(\frac{hw^3}{12}\right)_w \frac{\Phi_P - \Phi_w}{.5\Delta s_w} + \left(\frac{hw^3}{12}\right)_e \frac{\Phi_e - \Phi_P}{.5\Delta s_e} - \left(\frac{hw^3}{12}\right)_s \frac{\Phi_P - \Phi_s}{.5\Delta s_s} \\ & + \left(\frac{hw^3}{12}\right)_n \frac{\Phi_n - \Phi_P}{.5\Delta s_n} = 0 \end{aligned} \quad (52)$$

Material Balance at Fracture Intersections



$$T_w^f (\Phi_w^f - \Phi_P^f) + T_e^f (\Phi_e^f - \Phi_P^f) + T_s^f (\Phi_s^f - \Phi_P) + T_n^f (\Phi_n^f - \Phi_P) = 0$$

M97000883 C3

Figure 18. Fracture segment recharge points are labeled n, s, e, and w. Recharge at each of these fracture segment midpoints contributes to the mass balance at each fracture intersection.

where Δs_i is the length of segment i and $i = w, e, s, \text{ or } n$. The fracture transmissibility is defined by

$$TX_i^f = \left(\frac{hw^3}{12\Delta s} \right)_i \quad i = w, e, n, s. \quad (53)$$

Thus,

$$\begin{aligned} & 2TX_w^f (\Phi_w - \Phi_P) + 2TX_e^f (\Phi_e - \Phi_P) + 2TX_s^f (\Phi_s - \Phi_P) \\ & + 2TX_n^f (\Phi_n - \Phi_P) = 0 \end{aligned} \quad (54)$$

Equation 54 depends on the potential at the segment mid-points as well as node P, so the equation set has to be augmented by equations obtained by performing material balances on the fracture segments. Consider the segment e, for example. The material balance is

$$\begin{aligned} \frac{d}{dt} \int_{V_{fe}} \frac{1}{RT} \frac{p}{Z} dV = & - \left(\frac{hw^3}{12\mu} \right)_e \left(\frac{1}{RT} \frac{p}{Z} \frac{\partial p}{\partial s} \right)_{P-e} + \left(\frac{hw^3}{12\mu} \right)_e \left(\frac{1}{RT} \frac{p}{Z} \frac{\partial p}{\partial s} \right)_{E-e} \\ & + \frac{1}{RT} Q_r^{RC}(\Phi_e) + \frac{1}{RT} Q_l^{RC}(\Phi_e) \end{aligned} \quad (55)$$

where $\frac{1}{RT} Q_r^{RC}$ and $\frac{1}{RT} Q_l^{RC}$ are the molar recharge rates from the right and left sides of the fracture, respectively. Writing Equation 55 in terms of Φ yields

$$\frac{d}{dt} \int_{V_{fe}} \left(\frac{p}{Z} \right) dV = 2TX_e^f (\Phi_P - \Phi_e) + 2TX_e^f (\Phi_E - \Phi_e) + Q_r^{RC} + Q_l^{RC} \quad (56)$$

If the integral in Equation 56 is approximated by $V_{fe} \left(\frac{p}{Z} \right)_e$ and if the time derivative is approximated by a backward difference, we obtain

$$\begin{aligned} \frac{V_{fe}}{\Delta t_{n+1}} \left[\left(\frac{p}{Z} \right)_e^{n+1} - \left(\frac{p}{Z} \right)_e^n \right] = & 2TX_e^f (\Phi_P^{n+1} + \Phi_E^{n+1} - 2\Phi_e^{n+1}) \\ & + Q_r^{RC}(\Phi_e^{n+1}) + Q_l^{RC}(\Phi_e^{n+1}) \quad , \end{aligned} \quad (57)$$

where Δt_{n+1} is the time interval between t_n and t_{n+1} . Equations 54 and 57 are solved for Φ^{n+1} at the nodes and recharge points.

Equation 57 is nonlinear since $\left(\frac{p}{Z} \right)$, Q_r^{RC} , and Q_l^{RC} are nonlinear functions of Φ^{n+1} ; therefore, the set of Equations 54 and 57 is solved by the Newton Raphson technique. Thus, we define residuals by

$$\begin{aligned} R_P^{(k)} = & 2TX_w^f (\Phi_w^{(k)} - \Phi_P^{(k)}) + 2TX_e^f (\Phi_e^{(k)} - \Phi_P^{(k)}) \\ & + 2TX_s^f (\Phi_s^{(k)} - \Phi_P^{(k)}) + 2TX_n^f (\Phi_n^{(k)} - \Phi_P^{(k)}) \end{aligned} \quad (58)$$

and

$$\begin{aligned}
R_i^{(k)} &= 2TX_i^f \left(\Phi_P^{(k)} + \Phi_j^{(k)} - 2\Phi_i^{(k)} \right) + Q_r^{RC} \left(\Phi_i^{(k)} \right) \\
&+ Q_l^{RC} \left(\Phi_i^{(k)} \right) - \frac{V_{fi}}{\Delta t_{n+1}} \left[\left(\frac{p}{Z} \right)_i^{(k)} - \left(\frac{p}{Z} \right)_i^n \right] \\
i &= w, e, s, n \\
j &= W, E, S, N
\end{aligned} \tag{59}$$

where if $i = w$ then $j = W$, $i = e$, $j = E$, etc.

By applying the Newton-Raphson method to Equations 58 and 59, we obtain

$$\begin{aligned}
&2TX_w^f \left(\delta\Phi_w^{(k+1)} - \delta\Phi_P^{(k+1)} \right) + 2TX_e^f \left(\delta\Phi_e^{(k+1)} - \delta\Phi_P^{(k+1)} \right) \\
&+ 2TX_s^f \left(\delta\Phi_s^{(k+1)} - \delta\Phi_P^{(k+1)} \right) + 2TX_n^f \left(\delta\Phi_n^{(k+1)} - \delta\Phi_P^{(k+1)} \right) = -R_P^{(k)}
\end{aligned} \tag{60}$$

and

$$\begin{aligned}
&2TX_i^f \left(\delta\Phi_P^{(k+1)} + \delta\Phi_j^{(k+1)} - 2\delta\Phi_i^{(k+1)} \right) + \left(\frac{\partial Q_r^{RC}}{\partial \Phi} \right)_i^{(k)} \delta\Phi_i^{(k+1)} \\
&+ \left(\frac{\partial Q_l^{RC}}{\partial \Phi} \right)_i^{(k)} \delta\Phi_i^{(k+1)} - \frac{V_{fi}}{\Delta t_{n+1}} \frac{\partial}{\partial \Phi} \left(\frac{p}{Z} \right)_i^{(k)} \delta\Phi_i^{(k+1)} = -R_i^{(k)} \\
i &= w, e, s, n \\
j &= W, E, S, N
\end{aligned} \tag{61}$$

with

$$\Phi_l^{(k+1)} = \Phi_l^{(k)} + \delta\Phi_l^{(k+1)} \tag{62}$$

where Φ_l is the potential at any node or recharge point. Equations 60 and 61 are a set of linear equations, which can be solved in the following manner. Let

$$T_i^{RC} = - \left(\frac{\partial Q_r^{RC}}{\partial \Phi} \right)_i - \left(\frac{\partial Q_l^{RC}}{\partial \Phi} \right)_i + \frac{V_{fi}}{\Delta t_{n+1}} \frac{\partial}{\partial \Phi} \left(\frac{p}{Z} \right)_i \quad i = w, e, s, n \tag{63}$$

Then Equation 61 becomes

$$2TX_i^f \left(\delta\Phi_P^{(k+1)} + \delta\Phi_j^{(k+1)} \right) - \left(4TX_i^f + T_i^{RC} \right) \delta\Phi_i^{(k+1)} = -R_i^{(k)} \quad , \quad (64)$$

which can be solved to obtain

$$\delta\Phi_i^{(k+1)} = r_i R_i^{(k)} / 2TX_i^f + r_i \left(\delta\Phi_P^{(k+1)} + \delta\Phi_j^{(k+1)} \right) \quad (65)$$

where

$$r_i = 2TX_i^f / \left(4TX_i^f + T_i^{RC} \right) \quad . \quad (66)$$

Equations 65 and 66 were developed assuming that Φ_j^{n+1} is a variable to be solved for. If node j is a well node for a pressure controlled well, then Φ_j^{n+1} is a given value (boundary condition) rather than a variable; therefore, $\delta\Phi_j^{(k+1)} = 0$. In these cases, Equation 65 becomes

$$\delta\Phi_i^{(k+1)} = r_i R_i^{(k)} / 2TX_i^f + r_i \delta\Phi_P^{(k+1)} \quad (67)$$

and the expression for r_i remains the same. If node P is the first or last node on a fracture, then node j does not exist. In that case, the term $2TX_i^f(\Phi_j - \Phi_i)$ in Equation 56 is not present, and Equation 64 becomes

$$2TX_i^f \delta\Phi_P^{(k+1)} - (2TX_i^f + T_i^{RC}) \delta\Phi_i^{(k+1)} = -R_i^{(k)} \quad . \quad (68)$$

Solution of Equation 68 gives the same result as Equation 67 but with r_i given by

$$r_i = 2TX_i^f / (2TX_i^f + T_i^{RC}) \quad . \quad (69)$$

When the expressions for $\delta\Phi_i^{(k+1)}$ are combined with Equation 60, the following set of linear equations for the corrections at the nodes is obtained

$$A_P \delta\Phi_P^{(k+1)} + \sum_j A_j \delta\Phi_j^{(k+1)} = -(R_P^{(k)} + \sum_i r_i R_i^{(k)}) \quad (70)$$

where

$$A_p = 2\sum_i TX_i(r_i - 1) \quad (71)$$

and

$$\begin{aligned} A_j &= 2TX_i r_i && \text{if } \Phi_j \text{ is a variable} \\ A_j &= 0 && \text{if } \Phi_j \text{ is constant or does not exist.} \end{aligned} \quad (72)$$

The material balance at the well nodes is similar to the balance at a normal node except that the pressure (hence potential) is uniform for all nodes and recharge points that are a part of the well. For a pressure controlled well, the pressure is specified by the user and the total inflow to the well represents the production rate for the well. In the case of a rate controlled well, the total inflow to the well is required to sum to a user specified value (boundary condition) and the well potential is an unknown to be solved for. The well material balance is

$$\begin{aligned} \frac{d}{dt} \int_{V_H} \frac{1}{RTZ} p dV + \rho_{sc} Q_{Vsc} &= \sum_{k_s} (Q_r^{RC} / RT + Q_l^{RC} / RT)_{k_s} \\ + \sum_{j_f} &\left[\left(\frac{hw^3}{12} \right)_l \left(\frac{p}{Z\mu} \frac{dp}{ds} \right)_l - \left(\frac{hw^3}{12} \right)_r \left(\frac{p}{Z\mu} \frac{dp}{ds} \right)_r \right]_{j_f} \end{aligned} \quad (73)$$

where k_s is summed over the well segments, and j_f is summed over the intersecting fractures. In Equation 73, the integral represents the rate of gas accumulation in the horizontal well bore, ρ_{sc} is the molar density at standard conditions, and Q_{Vsc} is the volumetric flow rate measured at standard conditions. Expressing Equation 73 in terms of the potential and discretizing it yields

$$\begin{aligned} 2\sum_{j_f} [TX_r^f(\Phi_r - \Phi_w) + TX_l^f(\Phi_l - \Phi_w)]_{j_f} + \sum_{k_s} (Q_r^{RC} + Q_l^{RC})_{k_s} \\ - \frac{V_H}{\Delta t_{n+1}} \left[\left(\frac{p}{Z} \right)_w^{(n+1)} - \left(\frac{p}{Z} \right)_w^n \right] - Q_{comp} = 0 \end{aligned} \quad (74)$$

where Φ_w is the well potential, Φ_r and Φ_l are the potentials at the recharge points of the right and left segments of intersecting fractures, respectively. V_H is the volume of the horizontal wellbore and Q_{comp} is given by

$$Q_{comp} = p_{sc} T Q_{Vsc} / T_{sc} \quad (75)$$

Equation 74 replaces Equation 54 for well nodes of rate controlled wells. The residual corresponding to Equation 74 is

$$\begin{aligned}
 R_w^{(k)} = & 2\sum_{j_f} \left[TX_r^f \left(\Phi_r^{(k)} - \Phi_w^{(k)} \right) + TX_l^f \left(\Phi_l^{(k)} - \Phi_w^{(k)} \right) \right] \\
 & + \sum_{k_s} \left(Q_r^{RC} \left(\Phi_w^{(k)} \right) + Q_l^{RC} \left(\Phi_w^{(k)} \right) \right)_{k_s} \\
 & - \frac{V_H}{\Delta t_{n+1}} \left[\left(\frac{p}{Z} \right)_w^{(k)} - \left(\frac{p}{Z} \right)_w^n \right] - Q_{comp} \quad .
 \end{aligned} \tag{76}$$

By applying the Newton-Raphson technique to Equation 66, we obtain

$$\begin{aligned}
 & 2\sum_{j_f} \left[TX_r^f \left(\delta\Phi_r^{(k+1)} - \Phi_w^{(k+1)} \right) + TX_l^f \left(\delta\Phi_l^{(k+1)} - \delta\Phi_w^{(k+1)} \right) \right]_{j_f} \\
 & + \sum_{k_s} \left[\left(\left(\frac{\partial Q_r^{RC}}{\partial \Phi} \right)_w^{(k)} + \left(\frac{\partial Q_l^{RC}}{\partial \Phi} \right)_w^{(k)} \right) \delta\Phi_w^{(k+1)} \right]_{k_s} \\
 & - \frac{V_H}{\Delta t_{n+1}} \frac{\partial}{\partial \Phi} \left(\frac{p}{Z} \right)_w^{(k)} \delta\Phi_w^{(k+1)} = - R_w^{(k)} \quad .
 \end{aligned} \tag{77}$$

If we define

$$T_w^{RC} = - \sum_{k_s} \left(\left(\frac{\partial Q_r^{RC}}{\partial \Phi} \right)_w + \left(\frac{\partial Q_l^{RC}}{\partial \Phi} \right)_w \right)_{k_s} + \frac{V_H}{\Delta t_{n+1}} \frac{\partial}{\partial \Phi} \left(\frac{p}{Z} \right)_w \quad , \tag{78}$$

then Equation 77 can be written as

$$\begin{aligned}
 & 2 \sum_{j_f} \left[TX_r^f \left(\delta\Phi_r^{(k+1)} - \delta\Phi_w^{(k+1)} \right) + TX_l^f \left(\delta\Phi_l^{(k+1)} - \delta\Phi_w^{(k+1)} \right) \right]_{j_f} \\
 & - \left(T_w^{RC} \right)^{(k)} \delta\Phi_w^{(k+1)} = - R_w^{(k)} \quad .
 \end{aligned} \tag{79}$$

When Equations 65 and 67 are used for $\delta\Phi_r^{(k+1)}$ and $\delta\Phi_l^{(k+1)}$, then Equation 79 assumes a form similar to Equation 70 except that the sum is over all nodes that terminate fracture segments that intersect the wellbore. Thus, we can write

$$A_w \delta \Phi_w^{(k+1)} + \sum_j A_j \delta \Phi_j = - \left(R_w^{(k)} + \sum_{j_f} \left(r_r R_r^{(k)} + r_l R_l^{(k)} \right)_{j_f} \right) \quad (80)$$

where

$$A_w = 2 \sum_{j_f} \left[TX_r^f (r_r - 1) + TX_l^f (r_l - 1) \right]_{j_f} - T_w^{RC(k)} \quad (81)$$

and A_j is given by Equation 72.

After Equations 70 and 80 have been solved for $\delta \Phi_j^{(k+1)}$, then Equations 65 and 67 are used to calculate $\delta \Phi_i^{(k+1)}$. After the corrections are applied to $\Phi_j^{(k)}$, the residuals $\left(R_p^{(k+1)}, R_i^{(k+1)}, \text{ and } R_w^{(k+1)} \right)$ are tested to determine whether they meet the convergence criteria. If the criteria are not met, Equations 70 and 80 are solved for a new set of corrections, and the process is repeated until the equations have converged.

Equations 70 and 80 constitute a large sparse set of linear equations and any method suitable for this type of system can be used for their solution. The point over-relaxation method was chosen for this work. If we write the generic form for Equations 70 and 80 as

$$A_c \delta \Phi_c^{(k+1)} + \sum_j A_j \delta \Phi_j^{(k+1)} = I_c^{(k)} \quad (82)$$

where the sum is over all nodes coupled to node c, which is either a normal node or a rate controlled well bore and I_c is the appropriate sum of residuals, then the solution algorithm is

$$\delta \Phi_c^{l+1} = (1-\omega) \delta \Phi_c^l + \omega \left(I_c - \sum_j A_j \delta \Phi_j^l \right) / A_c \quad (83)$$

In Equation 83 the superscript denotes the iteration level of the linear solution technique, and ω is the over-relaxation parameter. The converged solution of Equation 83 corresponds to $\delta \Phi_c^{(k+1)}$, which is the $k+1$ correction to Φ_c in the Newton-Raphson technique. The over-relaxation parameter is chosen to minimize the average number of iterations required to solve Equation 82 subject to $1 < \omega < 2$.

Equations 58 and 59 are true regardless of the form of Q_r^{RC} and Q_l^{RC} . In this work they are calculated using a numerical one-dimensional unsteady model; however, any model that computes the recharge rate and its derivative as a function of the pressure history in the adjoining flow path could have been used. The following explains how Q^{RC} and $\partial Q^{RC} / \partial \Phi_0$ are computed in this work.

The numerical model for recharge requires dividing up the effective volume drained by a flow path into a set of discrete blocks (see Figure 19). If V_{eff} is the effective volume of a matrix block then the simplest model is

$$V_{eff} = \Delta s \ h \ x_{eff} \quad (84)$$

where Δs is the length of the flow path segment adjoining the volume, and x_{eff} is the effective length of the volume. Here the effective volume is chosen to have a rectangular plan, but other plans such as trapezoidal or triangular plans could have been chosen. The volume is divided into n_b subvolumes with unequal Δx 's. The volume adjacent to the fracture has the smallest Δx , the next volume has a Δx of β times the first, the next has a Δx of β times Δx of the second and so forth, so that

$$x_{eff} = \sum_{i=0}^{n_b-1} \Delta x_1 \beta^i \quad (85)$$

Performing the sum and solving for Δx_1 yields

$$\Delta x_1 = (\beta - 1) x_{eff} / (\beta^{n_b} - 1) \quad (86)$$

where n_b is chosen so that

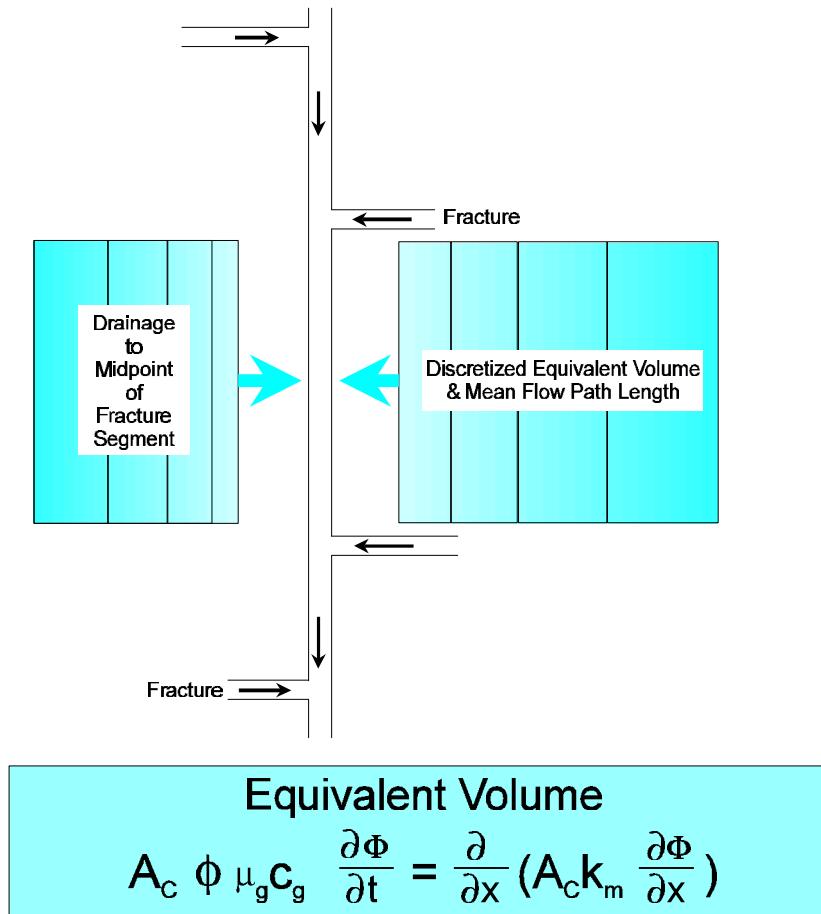
$$\Delta x_{scale} / \beta < \Delta x_1 \leq \Delta x_{scale} \quad (87)$$

when Δx_{scale} is computed from

$$\Delta x_{scale} = (\beta - 1) \max(x_{eff}) / (\beta^{n_{max}} - 1) \quad (88)$$

In Equation 88 $\max(x_{eff})$ means the largest value obtained for x_{eff} for any effective volume in the reservoir. This procedure results in all subvolumes adjacent to flow paths having approximately the same size Δx_1 regardless of the size of x_{eff} of the effective volume. Thus, those effective volumes with the largest x_{eff} are divided into n_{max} subvolumes while those with smaller x_{eff} are divided into fewer subvolumes. The combination of $\max(x_{eff})$, β , and n_{max} determines the spatial resolution of a simulation.

Idealization of Matrix Subregion Drainage



M97000880 C3

Figure 19. Matrix blocks of varying shapes and sizes are divided into subregions that are each approximated by a rectangular block of equivalent volume and mean flow path length. Flow within these subregions is represented by a one-dimensional unsteady-state model.

The equations solved in the matrix blocks are standard equations for quasi-one-dimensional flow as modified for porous media. To simplify notation, no subscripts are used to designate a particular effective matrix volume. Thus, for any effective volume we have

$$A_c(x) \frac{\partial}{\partial t} (\phi \rho) + \frac{\partial}{\partial x} (A_c(x) \rho \bar{u}) = 0 \quad (89)$$

where A_c is the local cross-sectional area of the system, ϕ is the porosity of the matrix rock, and \bar{u} is the superficial or darcy velocity. Substituting for ρ and using the fact that $\frac{1}{RT}$ is a constant gives

$$A_c \frac{\partial}{\partial t} \left(\phi \frac{p}{Z} \right) + \frac{\partial}{\partial x} \left(A_c \frac{p}{Z} \bar{u} \right) = 0 \quad (90)$$

When \bar{u} is given by Darcy's Law and use is made of the definition of Φ we obtain

$$A_c \frac{\partial}{\partial t} \left(\phi \frac{p}{Z} \right) - \frac{\partial}{\partial x} \left(A_c k_m \frac{\partial \Phi}{\partial x} \right) = 0 \quad (91)$$

where k_m is the matrix permeability. Equation 91 is the partial differential equation that models the equivalent one-dimensional systems.

The system is solved numerically by discretizing the effective matrix volume into n_b blocks centered at x_i with length Δx_i where $i=1, \dots, n_b$. The boundaries of block i are at $x_{i-1/2}$ and $x_{i+1/2}$. The discrete equations are obtained by integrating Equation 91 with respect to x from $x_{i-1/2}$ to $x_{i+1/2}$. Because the boundaries of the cells are fixed in time, this yields

$$\frac{d}{dt} \int_{x_{i-1/2}}^{x_{i+1/2}} A_c \phi \left(\frac{p}{Z} \right) dx - \left(A_c k_m \frac{\partial \Phi}{\partial x} \right)_{x_{i+1/2}} + \left(A_c k_m \frac{\partial \Phi}{\partial x} \right)_{x_{i-1/2}} = 0 \quad (92)$$

The integral in Equation 92 is approximated by $V_i \left(\frac{p}{Z} \right)_i$ where V_i is the pore volume of block i , while the flow terms are approximated by $\pm 2 (k_m A_c)_{i \pm 1/2} (\Phi_{i \pm 1} - \Phi_i) / (\Delta x_i + \Delta x_{i \pm 1})$ where the plus sign holds at $x_{i+1/2}$ and the minus sign at $x_{i-1/2}$. The expressions for the flow terms hold at all cell boundaries except $x_{1/2}$ and $x_{n_b+1/2}$. The flow at $x_{1/2}$ is given by $2 (k_m A_c)_{1/2} (\Phi_l - \Phi_o) / \Delta x_1$ where Φ_o is the boundary condition for this matrix block and is equal to the local value of Φ^f . The flow at $x_{n_b+1/2}$ is zero. If we define

$$TX_{1/2} = 2 (k_m A_c)_{1/2} / \Delta x_1 \quad (93)$$

$$TX_{i+1/2} = 2 (k_m A_c)_{i+1/2} / (\Delta x_i + \Delta x_{i+1}) \quad i=1, \dots, n_b-1 \quad (94)$$

$$TX_{n_b+1/2} = 0 \quad (95)$$

Then Equation 92 can be written as

$$\frac{d}{dt} \left[V_i \left(\frac{p}{Z} \right)_i \right] - TX_{i+1/2} (\Phi_{i+1} - \Phi_i) + TX_{i-1/2} (\Phi_i - \Phi_{i-1}) = 0 \quad (96)$$

$i = 1, \dots, n_b$

The finite difference equations for the matrix blocks are completed by using a backward difference for the time derivative,

$$\frac{1}{\Delta t_{n+1}} \left[V_i^{n+1} \left(\frac{p}{Z} \right)_i^{n+1} - V_i^n \left(\frac{p}{Z} \right)_i^n \right] - TX_{i+1/2} (\Phi_{i+1}^{n+1} - \Phi_i^{n+1}) + TX_{i-1/2} (\Phi_i^{n+1} - \Phi_{i-1}^{n+1}) = 0 \quad (97)$$

$i=1, \dots, n_b$

Unless the gas pressure is extremely high the change in pore volume with pressure is small compared to the gas compressibility; therefore, the V_i are treated as constants. The set of equations for Φ_i^{n+1} are non-linear since $\frac{p}{Z}$ is a non-linear function of Φ ; hence, the equations must be solved by iteration. The residuals for the equations are defined by

$$R_i^{(k)} = \frac{V_i}{\Delta t_{n+1}} \left[\left(\frac{p}{Z} \right)_i^{(k)} - \left(\frac{p}{Z} \right)_i^n \right] - TX_{i+1/2} (\Phi_{i+1}^{(k)} - \Phi_i^{(k)}) + TX_{i-1/2} (\Phi_i^{(k)} - \Phi_{i-1}^{(k)}) \quad (98)$$

$i=1, \dots, n_b$

where the superscript (k) denotes the kth iteration for the n+1 time level. The solution has been obtained when

$$R_i^{n+1} = 0 \quad .$$

Newton's method is used satisfy Equation 98; thus,

$$\begin{aligned}
R_i^{(k)} + \left(\frac{V_i}{\Delta t_{n+1}} \right) \left[\frac{\partial}{\partial \Phi_i} \left(\frac{p}{Z} \right) \right]^{(k)} \delta \Phi_i^{(k+1)} - TX_{i+1/2} \left(\delta \Phi_{i+1}^{(k+1)} - \delta \Phi_i^{(k+1)} \right) \\
+ TX_{i-1/2} \left(\delta \Phi_i^{(k+1)} - \delta \Phi_{i-1}^{(k+1)} \right) = 0 \quad i=1, \dots, n_b
\end{aligned} \tag{99}$$

where

$$\Phi_i^{(k+1)} = \Phi_i^{(k)} + \delta \Phi_i^{(k+1)} \tag{100}$$

and

$$\frac{\partial}{\partial \Phi_i} \left(\frac{p}{Z} \right)^{(k)} = \frac{\partial}{\partial p} \left(\frac{p}{Z} \right)_i^{(k)} \bigg/ \left(\frac{d\Phi}{dp} \right)_i^{(k)} = (\mu \ c_g)_i^{(k)} . \tag{101}$$

Once the Φ_i^{n+1} have been obtained, the term that represents the recharge rate is given by

$$Q^{RC} = TX_0 (\Phi_1 - \Phi_0) \tag{102}$$

where Φ_0 denotes the flow path potential at the recharge point. The sensitivity coefficient used in the solution of the flow path material balances is given by

$$\frac{\partial}{\partial \Phi_0} (Q^{RC}) = TX_0 \left(\frac{\partial \Phi_1}{\partial \Phi_0} - 1 \right) \tag{103}$$

An equation for $\frac{\partial \Phi_1}{\partial \Phi_0}$ is derived by differentiating Equation 97 at convergence with respect to

Φ_0 . This yields

$$\begin{aligned}
\left(\frac{V_i}{\Delta t_{n+1}} \right) \left[\frac{\partial}{\partial \Phi_i} \left(\frac{p}{Z} \right) \right]^{n+1} \left(\frac{\partial \Phi_i}{\partial \Phi_0} \right)^{n+1} - TX_{i+1/2} \left[\left(\frac{\partial \Phi_{i+1}}{\partial \Phi_0} \right)^{n+1} - \left(\frac{\partial \Phi_i}{\partial \Phi_0} \right)^{n+1} \right] \\
+ TX_{i-1/2} \left[\left(\frac{\partial \Phi_i}{\partial \Phi_0} \right)^{n+1} - \left(\frac{\partial \Phi_{i-1}}{\partial \Phi_0} \right)^{n+1} \right] = 0 \quad i=1, \dots, n_b .
\end{aligned} \tag{104}$$

This equation has the same set of coefficients as Equation 96, but a different right-hand side. The solution of the set of Equations 104 produces a value for $\partial\Phi_1/\partial\Phi_0$, which is used in Equation 103 to compute $\partial Q^{RC}/\partial\Phi_0$.

Project Description: NFFLOW

A FORTRAN program called NFFLOW implements the reservoir model presented above. The program reads two input files. One file contains the fracture network plus a description of the well. The other input file contains a physical description of the reservoir and recurrent data on output control and either well production or bottom-hole pressures. Output goes to four files. One output file contains a summary report of production and bottom-hole pressures. The second file, a plotable ASCII file, contains the gas pressures for each fracture segment. A third output file lists the input reservoir data, a node summary with flow path indices, the matrix volumes for each segment, and the simulation results. An optional output logs the computational processes at one of three levels of detail ((a) a nonlinear iteration report, (b) adds a linear solver report, (c) adds a report on the recharge models).

The standard well is a horizontal well. Horizontal wells are treated as infinitely conductive fractures (i.e., lines of constant pressure), so the productivity is strongly influenced by the number and quality of the fractures that it intersects. Vertical wells are modeled as very short horizontal well segments positioned to intersect fractures. Using a file editor, the user manually adds a well description plus any induced hydrofractures to the end of the file that contains the fracture network.

Fracture segment pressures are plotted or viewed with a program called PLOTIT. Colors are assigned nonlinearly to represent gas pressures within the fracture segments.

Results: Example Output, Validation, and Speed

We have used the flow simulator to simulate a well test (Branagan et al., 1988) that was performed on the MWX #1 well, Rulison Field, Colorado. The goal was to validate our simulator and fracture network models. Simulation would accomplish this if it could match bottom-hole pressures in the test well and in two nearby observation wells while simulating production over the duration of the variable rate drawdown and buildup phases of the well test. All previously published reservoir parameters (Branagan et al., 1987, 1988) were used; only fracture apertures were varied to produce a match. In all simulations, a short well lateral was used to connect the vertical well to the fracture nearest the center of the flow region. Aperture of the fracture nearest the flow region was varied to improve the match.

On average, the simulation results closely matched the test results for the buildup portion of the test but not the drawdown portion. Only a rough match could be obtained for the drawdown portion. Part of this problem seems to have resulted from our adherence to published values, which could slightly misrepresent the reservoir's true parameters. However, the other part may relate to NFFLOW: it needs to simulate water (or drilling fluid) obstruction of fractures near the well bore.

Despite its current inability to model two-phase flow, the flow simulator proved useful in the MWX study. Plots of fracture pressure proved helpful in assessing permeability anisotropy of the fracture network, pressure drop in the vicinity of the observation wells, and the connectivity of the fracture network proximal to the well. Plots of fracture pressure combined with pressure versus time plots enabled several specific conclusions regarding the existence of cross fractures, the lengths of fractures relative to those in the outcrop, the volume of reservoir tested, the minimum density of fractures, and the relative apertures of the fracture sets.

Results from one of the MWX simulations are presented as Figures 20 through 24. Of course, statistically equivalent networks give different flow responses, as shown in Figure 25; so several simulations are needed to determine the average result of any particular network model.

Flow simulator run times, for a case study with a network consisting of 2300 fractures and 51 time steps, were less than one hour when our VAX 8650 was unburdened. Parts of the code have been run on a Pentium 200 MHz computer to test performance. Processing took only 70 percent as much time on the Pentium, giving estimated run times of about 35 minutes on this computer.

Benefits

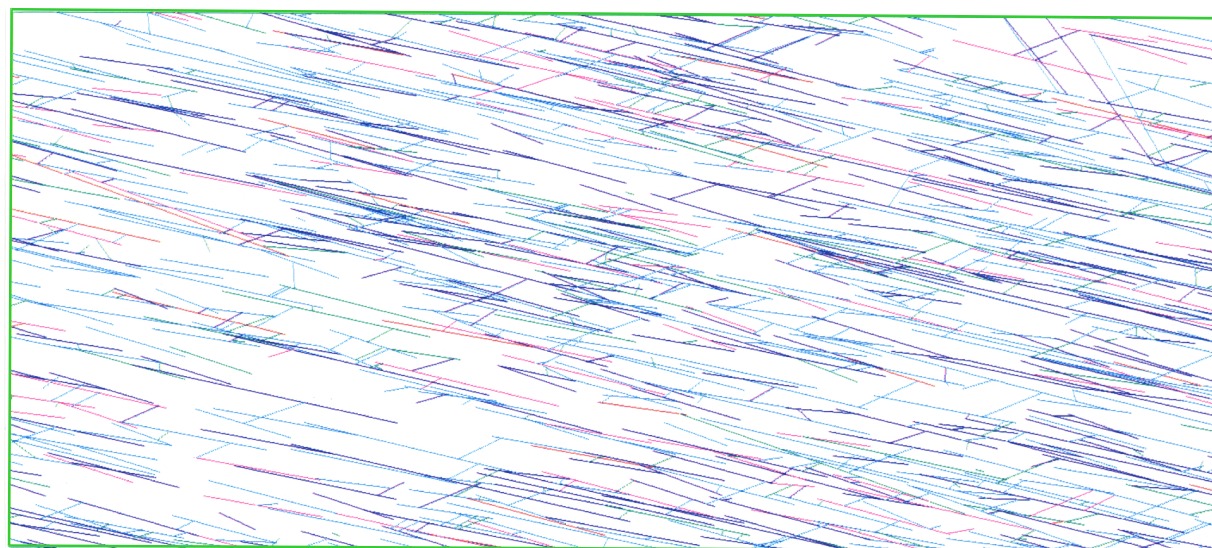
This project demonstrates that strata-bound tight reservoirs containing irregular, semidiscontinuous fracture networks can be simulated without gross simplification (e.g., regular grids of fractures), without statistical abstractions (i.e., equivalent permeability tensor maps), and without herculean efforts. *This project represents a significant advancement in the art of gas reservoir simulation by being among the first to readily simulate gas reservoir flow and drainage with a discrete, irregular, stochastic fracture network using a large number of fractures.*

Discrete stochastic fracture network models are superior to the currently popular anisotropic porous media models for modeling flow in small areas near the well bore. Furthermore, data analysis and modeling with fracture network statistics can require less effort than the abstraction process that is required to derive equivalent gridblock permeabilities for the anisotropic porous media models.

This flow simulator demonstrates that near-well-bore fracture network geometry can be accounted for without resort to "well functions," which translate grid-block variables into formation face variables for the well-bore.

This project improves our ability to analyze reservoirs. In other words, it presents a way of explaining reservoir behavior that could not be conclusively explained using conventional dual-porosity, dual-permeability reservoir simulators. For example, we determined that the lack of pressure response in the observation wells at the MWX site was merely the result of flow-testing the well over time periods that were too short. Previous investigators had contrived numerous plausible explanations (e.g., sealing faults, water blockage) but could say nothing with certainty.

Fracture Network



FRACTURE WIDTHS

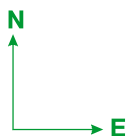
GREEN
0.0000246-0.0000426

CYAN
0.0000426-0.0000605

BLUE
0.0000605-0.0000784

PURPLE
0.0000784-0.0000964

RED
0.0000964-0.0001143



FLOW REGION
500.0 X 225.0

MWX4F1 DAY 3

Figure 20. This multicolored fracture pattern is a realization of our conceptual model of the fracture network in the paludal zone reservoirs of the Mesaverde Group, MWX test site, near Rifle, Colorado. The WNW fractures are the regional master fracture set observed in core and in nearby outcrops. The NE cross-fracture set represents our interpretation of three NE-oriented fractures in the SHCT-1 core (inclined) through the target reservoirs. Four NNW fractures seen in the NE corner of the plot are part of a low density set of shear fractures. A few random fractures were added. Total fracture density is 0.336 ft/ft^2 , which is produced by a total of 1161 fractures. There are 1846 intersections. Equivalent hydraulic apertures and flow region dimensions are shown in units of feet.

Unlike most previous irregular fracture-network flow (aquifer) simulators, this one models dynamic drainage and recharge of the matrix rock, simulates production either through multi-lateral horizontal wells or fractured vertical wells, operates in either rate-controlled or pressure-controlled modes, and plots the gas pressures in all the fracture segments of the network.

Fracture Reservoir

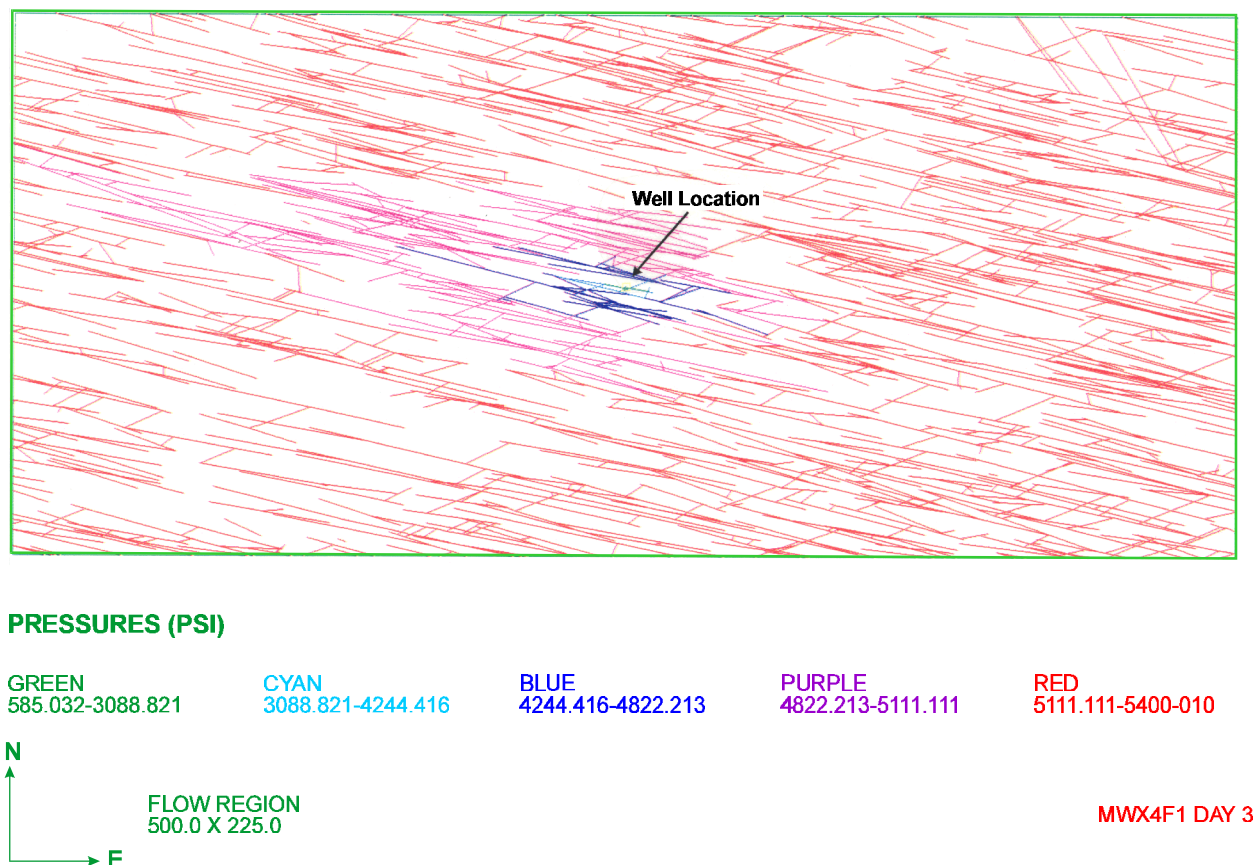


Figure 21. The pattern of gas pressure within fractures is illustrated with color in this plot. Overall, the color pattern represents the potentiometric surface, with its "cone of depression" around the well. This is day 3.0 during the simulation of the well test (see Figure 24) at the beginning of the main drawdown event. One master regional fracture intersects the well, and the aperture of this fracture was reduced (via trial and error testing) to 30.0×10^{-6} ft to improve the match between the simulation results and the test results. Drawdown occurs preferentially to the WNW of the well where local connectivity is better.

Suggested Future Activities

Future research and development of the fracture network generator should focus on using the full range of data available in the oil and gas industry. This means that the program must: (1) accept mapped fracture network attributes (e.g., fracture density maps), (2) condition the fracture network realizations to known fracture locations, (3) model compressional fold-related patterns and fault-related patterns around given fold axes and fault traces, (4) generate subseismic-scale folds and faults between known ones, and (5) correlate attributes (e.g., length-to-aperture correlation).

Fracture Reservoir

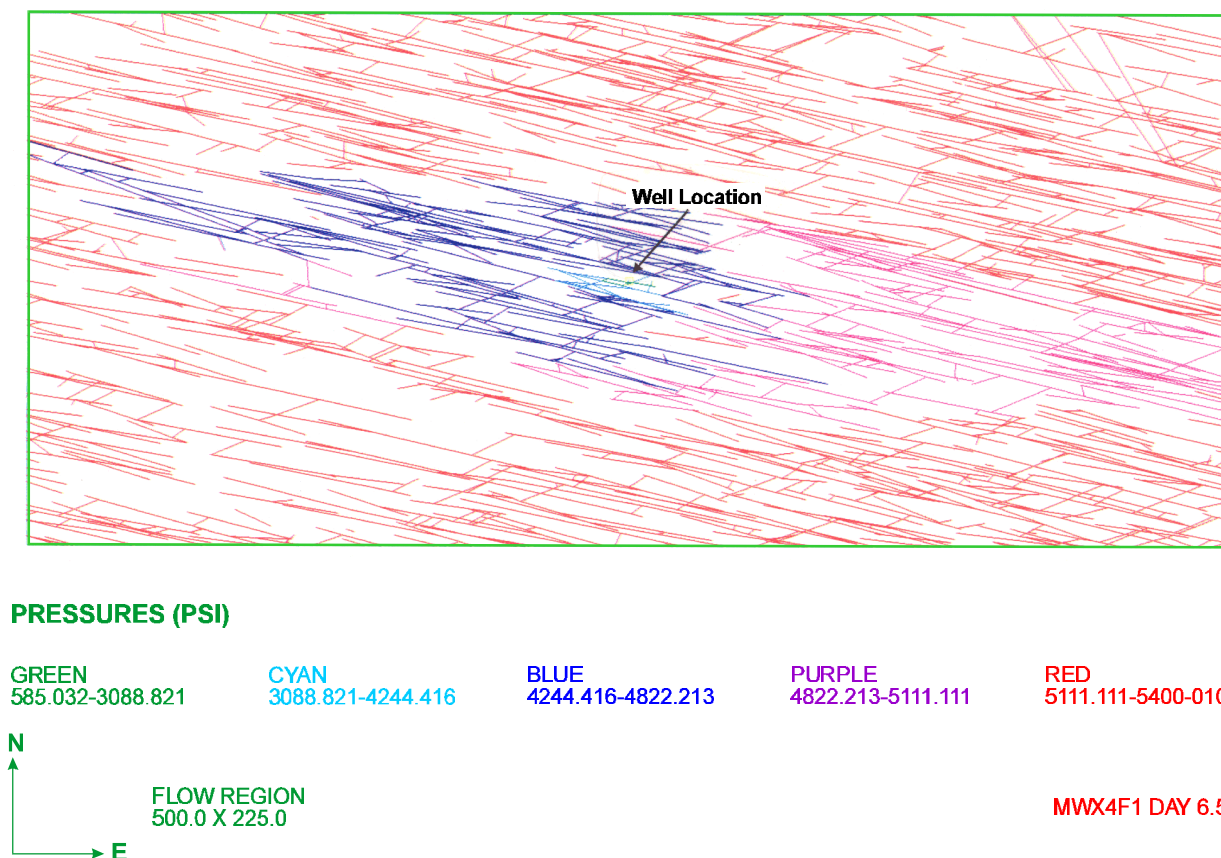


Figure 22. By day 6.5 during the simulation, the potentiometric depression has enlarged and spread to the ESE. This is at the time of maximum drawdown around the well. As shown by the comparison of this illustration with Figure 21, uneven drainage of apparently homogeneously fractured reservoirs can occur. Drainage from the NW stops because of low connectivity in that area. Far-field connectivity is better towards the east. Local connectivity and fracture density variations create subtle clustering, which affects reservoir drainage.

Additional work on the flow simulator should increase the number of fractures handled by it, model gas desorption/adsorption phenomena, model fracture apertures as a function of ambient fluid and rock pressures, and possibly accommodate two-phase flow.

References Cited

Batschelet, E., 1965. Statistical methods for the analysis of problems in animal orientation and certain biological rhythms. AIBS Monograph.

Fracture Reservoir

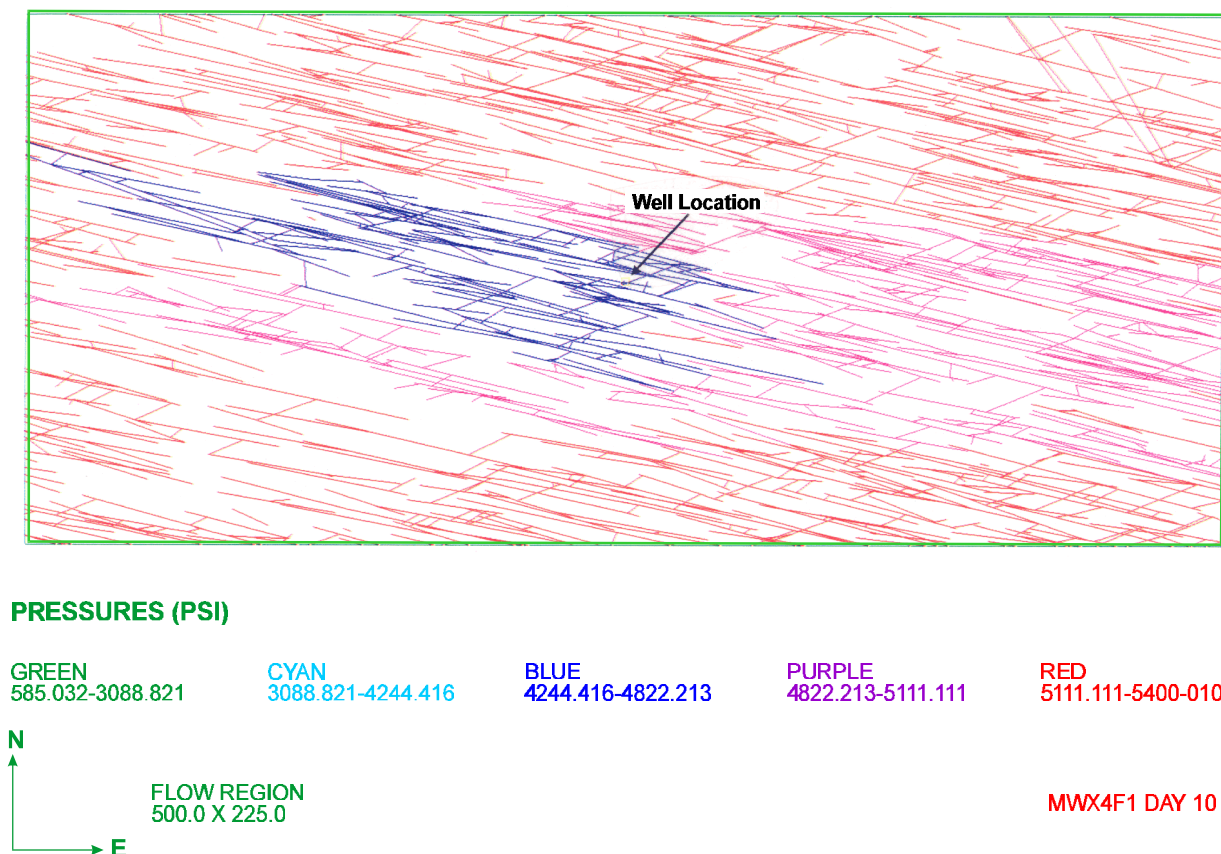


Figure 23. Day 10.0 occurs during the buildup phase of the well test. The potentiometric surface has flattened around the well (no green or cyan colors seen there), but the depression has spread further from the well.

Baecher, G.B., N.A. Lanney and H.H. Einstein, 1977. Statistical descriptions of rock properties and sampling. Proceedings of the 18th U.S. Symposium on Rock Mechanics. AIME, p.5C1:1-8.

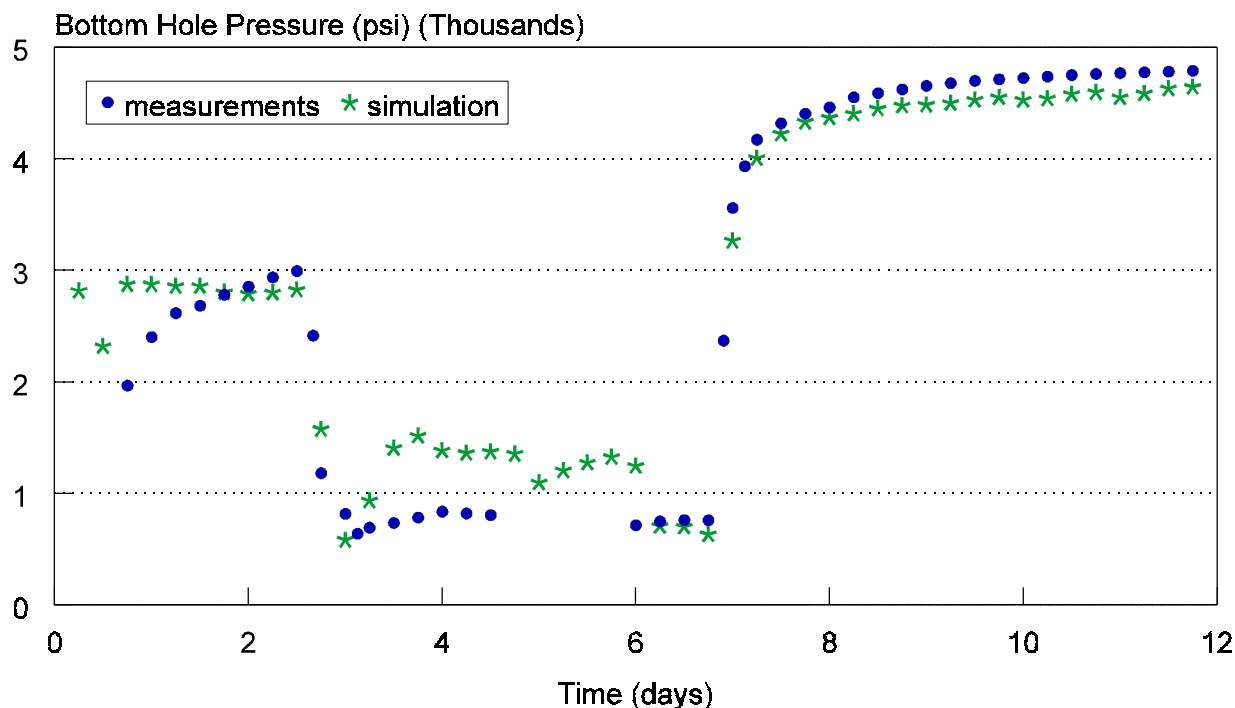
Branagan, P.T. 1988. Stimulation experiment -- zones 3 and 4: prefrac well testing. In: Multi-well Experiment Final Report: II, The Paludal Interval of the Mesaverde Formation. Sandia National Laboratories, Albuquerque, New Mexico, SAND88-1008, p. 8.1.1-8.1.22.

Branagan, P.T., C.L. Cipolla, S.J. Lee and L. Yan. 1987. Case history of hydraulic fracture performance in the naturally fractured paludal zone: the transitory effects of damage. Society of Petroleum Engineers, Richardson, Texas, SPE/DOE Paper 16397, p. 61-72.

Corbett, K., M. Friedman, D.V. Wiltschko and J.H. Hung, 1991. Controls on fracture development, spacing, and geometry in the Austin Chalk Formation, central Texas: considerations for exploration and production. American Association of Petroleum Geologists, 1991 Annual Convention, Dallas Geological Society Field Trip #4, Guidebook, 48 pp.

MWX-1 Well Test & Simulation Results

Level 4 Stochastic Fracture Network



Run MWX4F1a

Figure 24. Flow simulation results shown here are compared to the actual well test results. By adjusting matrix permeability and matrix porosity, along with developing an ability to simulate two-phase flow (the well initially produced some water), we could have improved the match. We used published values for matrix permeability and porosity, as measured in core and wire-line logs. The slight mismatch during the buildup phase results from boundary effects (we intentionally simulated a small area so the individual fractures would be readily visible in our plots), possibly combined with a slight lack of connectivity at distances of 50 to 100 ft from the well (notice lack of purple color around NW side of the potentiometric depression in Figure 23).

Finley, S.J. and J.C. Lorenz, 1988. Characterization of natural fractures in Mesaverde core from the multiwell experiment. Sandia National Laboratories, Albuquerque, New Mexico, SAND88-1800, 125 pp.

Gervais, F., J.P. Chiles and S. Gentier, 1995. Geostatistical analysis and hierarchical modeling of a fracture network in a stratified rock mass. In: Myer, Cook and Goodman and Tsang (eds.), Fractured and Jointed Rock Masses. A.A. Balkema, Rotterdam, p. 153-159.

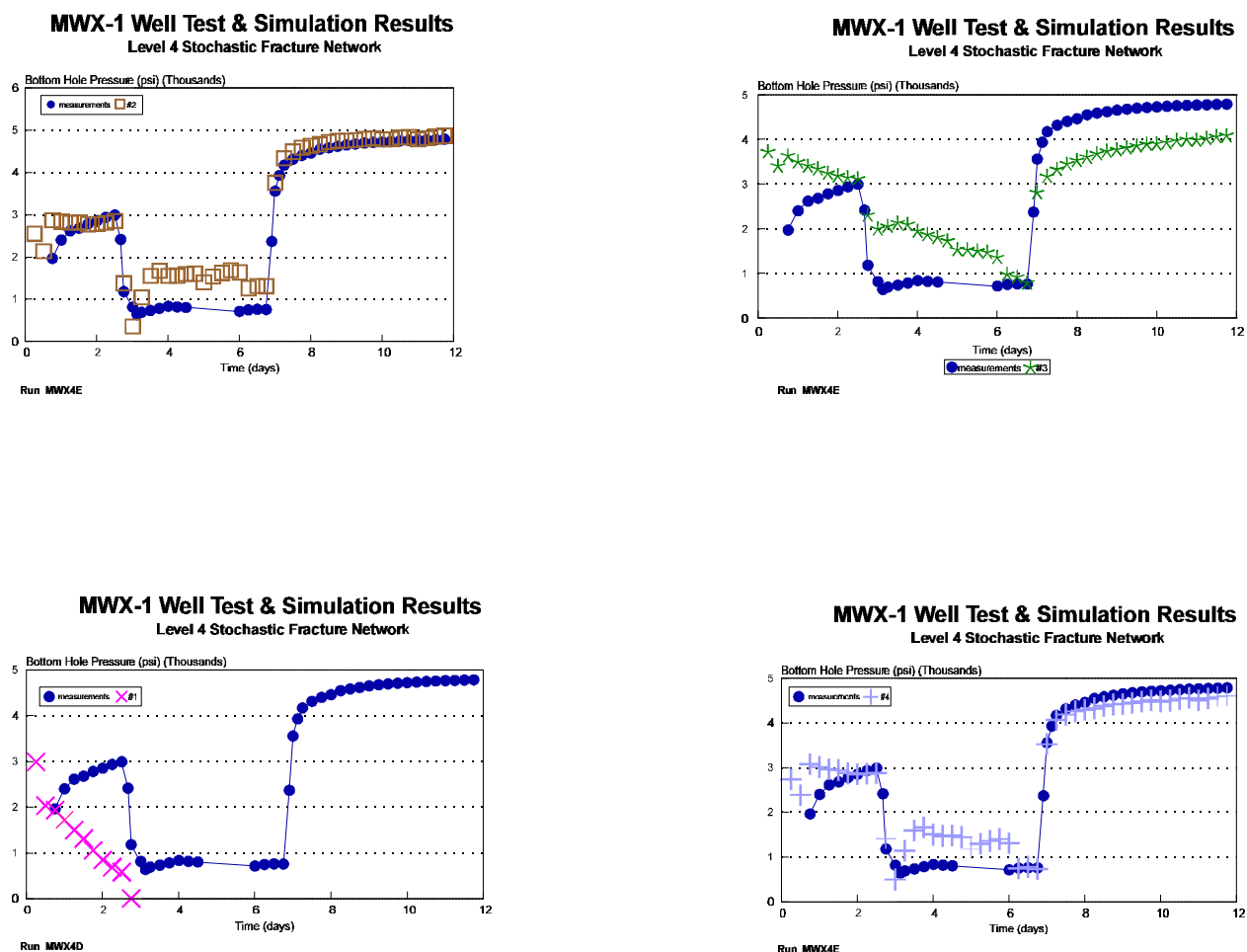


Figure 25. Statistically equivalent networks MWX4E2, -3, -4 show different pressure drawdown and buildup behavior as a function of the apertures and connectivity of the network around the well. Network MWX4D1 (bottom left) contained an additional set of cross fractures and a greater fracture density, but it lacked connectivity near the well.

Laubach, S.E., 1992. Fracture networks in selected cretaceous sandstones of the Green River and San Juan Basins, Wyoming, New Mexico, and Colorado. In: J.W. Schmoker, E.B. Coalson and C.A. Brown (eds.), *Geological Studies Relevant to Horizontal Drilling: Examples from Western North America*. Rocky Mountain Association of Geologists, p. 115-127.

Long, J.C.S., J.S. Remer, C.R. Wilson and P.A. Witherspoon, 1982. Porous media equivalents for networks of discontinuous fractures. *Water Resources Research*, vol. 18, no. 3, p. 645-658.

Lorenz, J.C., and S.J. Finley, 1991. Regional fractures II: fracturing of Mesaverde reservoirs in the Piceance Basin, Colorado. *The American Association of Petroleum Geologists Bulletin*, vol. 75, no. 11, p. 1738-1757.

Lorenz, J.C., N.R. Warpinski, P.T. Branagan and A.R. Sattler, 1989. Fracture characteristics and reservoir behavior of stress-sensitive fracture systems in flat-lying lenticular formations. *Journal of Petroleum Technology*, vol. 41, p. 615-622.

Overbey, Jr., W.K., R.S. Carden and J.N. Kirr, 1987. Recovery efficiency test project, phase I -- activity report, volume I: site selection, drill plan preparation, drilling, logging and coring operations. BDM Corporation, Morgantown, West Virginia, Report to DOE/METC.

Robinson, B.A., 1989. A fracture network model for water flow and solute transport. Los Alamos National Laboratories, New Mexico, rpt. no. LA-UR-89-11, 20 pp.

EXPLANATIONS OF VARIABLES FOR FRACTURE NETWORK GENERATOR

(variables not listed are explained in Table 5 or where used)

a	lower limit of range.
b	upper limit of range.
b_i	correction for variance in fracture orientation.
D_f	two-dimensional fracture density; average length of fracture trace per unit area (ft/ft ²).
D_{fci}	maximum two-dimensional intracluster fracture density; average length of fracture trace per unit area within a cluster where end effects do not exist. The representative sample area extends across the width of a cluster (ft/ft ²).
$D_{fci}(x)$	two-dimensional intracluster fracture density at location x (coordinate parallel to the axis of a cluster).
$l_{i,3.0}$	$\exp(U - 3s_u)$
$l_{i,2.0}$	$\exp(U + 2s_u)$
$l_{i,3.0}$	$\exp(U + 3s_u)$
L_{wi}	width of cluster box in set i .
n	number of events or objects, except where otherwise specified.
$N_{i,k}$	number of fractures in k th cluster of i th set.
$p(x)$	probability (density) function.
$P(x)$	probability distribution function.
q	number of equal-size quadrats or intervals of sample space.
R	random variate ($0 < R \leq 1.0$).
s	a general symbol for the standard deviation for any distribution that is indicated by a subscript.
U	arithmetic average of the natural logarithms of observations.
z	standard normal deviate.
γ	weight applied to calculate a weighted average.
ζ	degree of clustering in percent for the range between perfectly random locations to tight clustering in which all events occur in one interval of sample space. Accuracy is dependent on number of intervals used.
θ_{\max}	$\theta_i + 3 s_\theta$
θ_{\min}	$\theta_i - 3 s_\theta$
κ	weight applied to calculate a weighted average.
Λ_i	linear density of fractures (average number of fractures per unit length of a sample line normal to the mean orientation of the fractures) = $\lambda_i / \cos(\phi_i)$.
λ_i	fracture frequency (the average number of fractures per unit length of sample line).
Λ_{ci}	linear density of clusters (average number of clusters per unit length of a sample line normal to the mean orientation of the clusters) = $\lambda_{ci} / \cos(\phi_i)$.
λ_{ci}	cluster frequency (the average number of clusters per unit length of sample line).
ϕ_i	angle between the sample line and the normal pole of the fracture set (degrees).
χ	a general symbol for the mean value of x .

EXPLANATIONS OF VARIABLES FOR FLOW SIMULATOR

$A_c =$	Cross sectional area used in one-dimensional model.
$c_g =$	Gas compressibility.
$h =$	Formation thickness.
$k_m =$	Matrix permeability.
$n_b =$	Number of blocks in a specific one-dimensional model.
$n_{\max} =$	Maximum number of blocks in one-dimensional models.
$p =$	Gas pressure.
$Q_1^{RC}, Q_r^{RC} =$	Recharge rates as defined in Equation 9.
$Q_{\text{comp}} =$	Scaled surface production rate.
$Q_v =$	Volumetric flow rate.
$R =$	Universal gas constant.
$r =$	Ratio of transmissibilities defined by Equations 20 and 23.
$s =$	Distance along fracture.
$T =$	Absolute temperature.
$t =$	Time.
$T^{RC} =$	Sensitivity coefficient for recharge.
$TX^f =$	Fracture transmissibility as defined in Equation 7.
$\bar{u} =$	Darcy or superficial velocity.
$V_{\text{eff}} =$	Effective volume of a matrix block.
$V_f =$	Volume of fracture segment.
$V_H =$	Volume of horizontal wellbore segment.
$V_i =$	Volume of block i in one-dimensional model.
$w =$	Width of fracture aperture.
$x =$	Distance variable in one-dimensional models.
$x_{\text{scale}} =$	Scale length for one-dimensional models.
$Z =$	Gas Z-factor.
$\beta =$	Geometric ratio for non-uniform grid in one-dimensional models.
$\mu =$	Gas viscosity.
$\rho =$	Gas molar density.
$\Phi =$	Real gas pseudopotential.
$\phi =$	Matrix porosity.
$\omega =$	Over-relaxation parameter.

Superscripts

$k =$	Newton-Raphson iteration level.
$l =$	Iteration level in point over-relaxation method.
$n =$	Time level.

Subscripts

$c =$	Generic central node (either normal or well node).
$i =$	Recharge point for flow path. Block index in one-dimensional model.
$j =$	Node index.
$j_f =$	Intersecting fracture index.
$k_s =$	Well segment index.
$l =$	Left side of flow path.
$P =$	Normal node index.
$r =$	Right side of flow path.
$sc =$	Standard conditions.
$w =$	Well.